TECHNISCHE UNIVERSITÄT WIEN
INSTITUTE OF HIGH ENERGY PHYSICS,
AUSTRIAN ACADEMY OF SCIENCES

Masterthesis

From Dark to Light, Ionization and Heat. An Inquiry concerning the Complementary of Dark Matter Electron and Dark Matter Nuclear Scattering

Valentin Jan Czamler
1326617

Supervisor:

Prof. Dr. Jochen Schieck

Co-Supervisors:

Dr. Suchita Kulkarni

Dr. Florian Reindl

2021

Abstract

The recent development of direct detection experiments can be divided into two main approaches: On the one hand, to give weakly interacting massive particles (WIMPs) as Elizabeth Gibney puts it "a final chance to reveal itself" [71], on the other hand, to reach out for candidates beyond the WIMP-paradigm. In this regard, new possibilities in the search for dark matter arise by simultaneously lowering detection thresholds successively and exploiting new kinds of atomic or nuclear phenomena besides the well known **dark matter nucleus scattering**, namely **dark matter electron scattering**, **the Migdal effect** or **Bremsstrahlung**. While the interaction of dark matter particles and target materials differs for each effect, the observable quantity for each of these phenomena ultimately is the energy deposited in the detector. For dark matter nucleus scattering, some of the kinetic energy of a dark matter particle is transferred to the nucleus of a Standard Model particle. This energy deposition is then converted to measurable signals i.e. ionization, scintillation light or heat. The Migdal effect on the other hand induces ionization signals in addition to the nuclear recoil (3-body process), when a sub-GeV dark matter particle scatters off the nucleus. Finally, when dark matter couples directly to electrons (i. e. electron scattering), ionization and excitation in the electron system of the target atoms can be detected.
This means that, depending on the dark matter mass and its coupling to the Standard Model particles, a variety of detection avenues exist at direct detection experiments. The deposited energy of dark matter particles within the detector can mainly (with the exeption of bubble chambers) be measured via scintillation, ionization or heat. Understanding the limits of each effect therefore becomes a key aspect of exploiting the complete potential of current and future direct detection experiments. This is especially the case for dark matter scenarios that go beyond the WIMP paradigm by involving e.g. multiple components.

This thesis addresses a comprehensive analysis of the above described dominating theoretical effects induced by dark matter interaction with the Standard Model constituents, primarily taking liquid Xenon as an example. In order to achieve this, the astrophysical parameters, the possible ways of interaction and the detector response for each interaction need to be computed. This results in anticipated interaction rates for each effect and detec-

tor. Comparing these anticipated detection rates allows us to draw conclusions for possible blind spots and challenges in setting direct detection limits for particular dark matter scenarios.

Zusammenfassung

Wenn man so will, lässt sich die jüngere Entwicklung von Experimenten zum direkten Nachweis dunkler Materie (direct detection experiments) durch zwei wesentliche Linien charakterisieren: Einerseits wird versucht, den schwach wechselwirkenden massiven Teilchen (WIMPs), wie Elizabeth Gibney es ausdrückt, "eine letzte Chance [zu] geben, sich zu offenbaren" [71]. Andererseits hält man nach dunkle Materie-Kandidat*innen jenseits des WIMP-Paradigmas Ausschau. In diesem Zusammenhang eröffnen sich neue Möglichkeiten bei der Suche nach dunkler Materie, indem gleichzeitig sukzessive die Nachweisschwellen gesenkt und neben der **nuklearen Streuung** neuartige atomare bzw. nukleare Phänomene ausgenutzt werden, nämlich **Dunkle-Materie-Elektronenstreuung**, **der Migdal-Effekt** oder **Bremsstrahlung**.

Während sich die Wechselwirkungen von Dunkle-Materie-Teilchen und den Detektormaterialien für jeden Effekt unterscheiden, ist die beobachtbare Größe für jedes dieser Phänomene letztendlich die im Detektor deponierte Energie. Bei der Kernstreuung von Dunkler Materie wird ein Teil der kinetischen Energie eines Dunkle-Materie-Teilchens auf den Kern eines Standardmodell-Teilchens übertragen. Diese Energiedeposition wird dann in messbare Signale umgewandelt, d. h. in Ionisation, Szintillationslicht oder Wärme. Der Migdal-Effekt hingegen induziert zusätzlich zum Kernrückstoß (3-Körper-Prozess) Ionisationssignale, wenn ein sub-GeV-Dunkelmaterieteilchen am Kern abstreut. Wenn schließlich Dunkle Materie direkt an Elektronen koppelt (Elektronenstreuung), können Ionisation und Anregung im Elektronensystem der Detektormaterialien nachgewiesen werden.
Das bedeutet, dass direkte Nachweisexperimente heute mit der Situation konfrontiert sind, dass zahlreiche mögliche Wechselwirkungen zwischen dunkler Materie und den Detektormaterialien entscheidend begrenzten Methoden zu deren Nachweis gegenüber stehen. Die deponierte Energie von Dunkle-Materie-Teilchen im Detektor kann nur sehr begrenzt gemessen werden, nämlich über Szintillation, Ionisation oder Wärme. Das Verständnis der Grenzen jedes Effekts wird daher zu einem Schlüsselaspekt, um das gesamte Potenzial aktueller und zukünftiger Experimente zum direkten Nachweis dunkler Materie auszuschöpfen. Dies gilt insbesondere für Dunkle-Materie-Szenarien, die über das WIMP-Paradigma hin-

ausgehen oder mehrere Komponenten beinhalten.

Diese Arbeit befasst sich mit einer umfassenden Analyse der oben beschriebenen dominierenden theoretischen Effekte, die durch die Wechselwirkung der Dunklen Materie mit den Konstituenten des Standardmodells hervorgerufen werden, wobei primär flüssiges Xenon als Beispiel dient. Dazu müssen die astrophysikalischen Parameter, die möglichen Wege der Wechselwirkung und die initiale Detektor-Antwort für jede Wechselwirkung berechnet werden. Daraus ergeben sich die erwarteten Interaktionsraten für jeden Effekt und jeden Detektor. Der Vergleich dieser erwarteten Interaktionsraten erlaubt es, Rückschlüsse auf mögliche blinde Flecken und Herausforderungen bei der Festlegung von direkten Nachweisgrenzen für bestimmte Szenarien der Dunklen Materie zu ziehen.

Contents

Chapter 1

Dark Matter

The question of the nature of dark matter is surely one of the most pressing questions of modern cosmology as well as modern particle physics. Unless modern day physics is completely misled by its data sets, there is no doubt that it pervades the universe and yet it has not been detected directly. Modern cosmological observations have constituted a sophisticated exploration of the distribution of dark matter, which is confirmed to be the dominant component of the universe's matter content relative to ordinary, baryonic matter. Modern day particle physics came up with elaborate theories of dark matter and its possible interactions. In this sense, the physics of dark matter ranges from sub-atomic scales to that of the whole universe. This chapter briefly reviews major astronomic observations as well as theoretical considerations yielding evidence for the existence of dark matter, including their modern cosmological framework. By doing so, the author tries to preserve the timeline in order to display the historic evolution of the theory of dark matter. This is, however, compromised at some points, due to the specific angle this work takes in the discourse of dark matter. For a detailed review of the history of dark matter from a physicist's point of view, consider [57] and especially [40]. This Tour de Force through the history of dark matter shall be concluded with a brief outline of possible dark matter particle candidates, to finally draw attention to the possible detection.

1.1 A brief Prehistory of Dark Matter

The hypothesis and resulting theory of dark matter has an elaborate history. Lord Kelvin, the famous Scots-Irish physicist after whom the temperature scale is named, was among the first who tried to calculate the mass of our galaxy using estimates drawn from the observed velocity dispersion of visible stars [40]. Since Kelvin observed a discrepancy between the calculated mass and the stars he was able to see, he concluded: "Many of our stars, perhaps

a great majority of them, may be dark bodies." [126, 274]
The expression "dark matter" or "matière obscure" in the writing's French original was first mentioned by Henri Poincaré in his article *The Milky Way and the Theory of Gases* [106]. Poincaré disagrees with Kelvin's conclusions: "There are the stars which we see because they shine; but might there not be obscure stars which circulate in the interstellar space and whose existence might long remain unknown? Very well then, that which Lord Kelvin's method would give us would be the total number of stars including the dark ones; since his number is comparable to that which the telescope gives, then there is no dark matter, or at least not so much as there is of shining matter" [106]. During the following decades the dynamical evidence accumulated: The Estonian astronomer Ernst Öpik published a model of the motion of stars in the Galaxy in 1915, concluding that the presence of large amounts of unseen matter was rather unlikely [140]. In 1922, the Dutch astronomer Jacobus Kapteyn offered the first quantitative model for the shape and size of the Galaxy. [82] Similar to Öpik, he established a relationship between the motion of stars and their velocity dispersion. However in contrast to him he explicitly addressed the problem of dark matter. Further studies of the vertical kinematics of stars in the solar neighborhood as well the local dark matter density followed by Jan Oort (1932) [102]. With it, he extended existing estimates of James Jeans (1922) [80] and Bertil Lindblad (1926) [93], though yielding inconclusive and incompatible results (e.g. review [57]).
Dark matter is introduced to the scientific discourse as a term describing non-visible and gravitationally interacting matter. However, in the early astronomical discourse, dark matter was thought to likely consist of faint stars. It therefore could be accounted for through extrapolations and adaptions of the stellar mass function, i.e. the number density of galaxies as a function of their stellar mass, along with "nebulous" and "meteoric" matter [40]. While these options have been successively ruled out, the underlying nature of dark matter remains one of the grand mysteries of present-day physics.

1.2 Cosmological Framework

The history of dark matter is accompanied by several major changes of paradigm in our image of the universe. Today it is shaped by the *Big Bang Theory*, which assumes that the universe was formed in an extremely hot phase about 14 billion years ago, expanding ever since. This section tries to briefly outline the cosmological basis of the search for dark matter within direct detection experiments. In this regard, two principles are of particular importance:

a) The *cosmological principle* states that the Universe is isotropic and homogeneous on very large scales. There is neither a special point nor a special spatial direction within space-time, galaxies are evenly distributed with respect to their position and their angular directions on large scales.

b) *Gravitation* dominates the behavior of celestial bodies on large scales. This goes along with assuming an overall electrically neutral Universe. It is only against this background that the question of dark matter gains a particular interest.

We know that the cosmological principle is not true at small scales. The planet, solar system and Galaxy we inhabit are apparently inhomogeneous. Still, it provides a more or less simple model of the Universe allowing us to study its evolution.
The *relativistic Doppler Effect* describes how spectral lines of receding galaxies are shifted to longer wavelengths. In 1929, Edward Hubble measured the red-shifts of spectral lines of galaxies at various distances and found that all galaxies move away from the Milky Way with only a few exceptions for very close ones [77]. The derived Hubble's law describes the relation between the distance to a galaxy d and its velocity v:

$$v = H_0 d\,. \tag{1.1}$$

with H_0 being the Hubble constant. At first glance, this seems to violate the cosmological principle, since the velocities get bigger with increasing distance. This changes, however, if one takes into account the properties of space-time. In that regard, it is worth mentioning that two years before Hubble, Georges Lemaître had already found an explanation for this behaviour with his postulate of an expanding universe [89].

A scale factor $a(t)$ at a given time t allows to rewrite the Hubble's law:

$$v = \underbrace{\frac{\dot{a}(t)}{a(t)}}_{H(t)} d\,. \tag{1.2}$$

$H(t)$ could then be understood as the universe's expansion rate. In order to account this, one has to consider Einstein's General Theory of Relativity, in particular the Einstein field equation: [1]

$$G_{\mu\nu} + \Lambda g_{\mu\nu} = \kappa T_{\mu\nu}\,. \tag{1.3}$$

Where $G_{\mu\nu}$ is the Einstein-tensor describing the curvature of space-time, $g_{\mu\nu}$ is the metric

[1] For a more elaborate discussion of the Einstein field equation consider [74].

tensor, $T_{\mu\nu}$ is the stress-energy tensor, Λ the cosmological constant and κ the Einstein gravitational constant.[2] The Einstein gravitational constant is defined as:

$$\kappa = \frac{8\pi G}{c^4} \tag{1.4}$$

resulting in the stress-energy tensor components have units of energy density. The cosmological constant Λ was originally introduced to counterbalance the effects of gravity and achieve a static universe [58]. Einstein abandoned this concept, however, after Hubble's observation. Between then and the late 1990s, Λ was thought to be zero. Today, multiple theoretical considerations point to a non-zero positive cosmological constant, for a broader discussion consider [112]. Without going into further detail, it shall be noted that the Einstein field equation allows relating the curvature of space-time as determined by the metric with its matter–energy content. This provides the basis for further considerations: By finding a suitable metric the matter-energy content of the universe can be calculated. One such metric is the Friedmann–Lemaître–Robertson–Walker (FLRW) metric, which represents an exact solution of the Einstein field equation. This leads to the Robertson-Walker form of the line element:

$$\mathrm{d}s^2 = c^2\mathrm{d}t^2 - a(t)^2\left(\frac{\mathrm{d}r^2}{1-k\,r^2} + r^2(\mathrm{d}\theta^2 + \sin^2\mathrm{d}\Phi^2)\right) \tag{1.5}$$

with the scale factor $a(t)$ and the curvature k $(k = +1, 0, -1)$. This represents a homogeneous and isotropic model of the universe. For $k = 0$,the spatial hyper-surfaces are Euclidean and are called *flat* models [74, 271]. Setting a general form of the energy-momentum tensor with respect to *homogeneity* and *isotropy*:

$$T_{\mu\nu} = (\rho + p)u_\mu u_\nu + p g_{\mu\nu} \tag{1.6}$$

allows to solve the Einstein field equation. Here, ρ is the proper energy-mass density and p its pressure. Given homogeneity and isotropy as well as the Robertson-Walker line

[2] The Einstein-tensor can be written as the difference between the Ricci curvature-tensor $R_{\mu\nu}$ and the scalar curvature R multiplied with the metric tensor $g_{\mu\nu}$, resulting in $G_{\mu\nu} = R_{\mu\nu} - \frac{1}{2}Rg_{\mu\nu}$.

element this energy-momentum tensor contracts to a diagonal form:

$$(T_{\hat{\mu}\hat{\nu}}) = \begin{pmatrix} \rho & 0 & 0 & 0 \\ 0 & p & 0 & 0 \\ 0 & 0 & p & 0 \\ 0 & 0 & 0 & p \end{pmatrix}, \tag{1.7}$$

leading to the famous *Friedmann equations*:

$$\frac{\dot{a}^2 + kc^2}{a^2} = \frac{8\pi G\rho + \Lambda c^2}{3} \tag{1.8}$$

$$\frac{\ddot{a}}{a} = -\frac{4\pi G}{3}\left(\rho + \frac{3p}{c^2}\right) + \frac{\Lambda c^2}{3}. \tag{1.9}$$

These can be re-written into:[3]

$$H^2 = \left(\frac{\dot{a}}{a}\right)^2 = \frac{8\pi G}{3}\rho - \frac{kc^2}{a^2} + \frac{\Lambda c^2}{3} \tag{1.10}$$

$$\dot{H} + H^2 = \frac{\ddot{a}}{a} = -\frac{4\pi G}{3}\left(\rho + \frac{3p}{c^2} + \frac{\Lambda c^2}{4\pi G}\right). \tag{1.11}$$

For $k = 0$ (a flat universe) and $\Lambda = 0$ one could now define a critical density:

$$\rho_c = \frac{3{H_0}^2}{(8\pi G)}. \tag{1.12}$$

The densities relative to the critical density are called the *density parameters* or the *relative densities*, i. e.

$$\Omega_i = \frac{\rho_i}{\rho_c}. \tag{1.13}$$

The most important contributions to the total density parameter Ω arise from radiation Ω_γ, matter Ω_m and possibly the cosmological constant Ω_V. Leading to $\Omega = \Omega_\gamma + \Omega_m + \Omega_V$. By additionally defining the spatial curvature parameter (Ω_k):

$$\Omega_k = \frac{-kc^2}{{H_0}^2{a_0}^2} \tag{1.14}$$

[3] for a more detailed derivation consider again [74].

the Friedmann equation takes the form:

$$\Omega + \Omega_k = 1\,. \tag{1.15}$$

This leads to an open model $\Omega_k < 0$, a flat model $\Omega_k = 0$ and a closed model $\Omega_k > 0$:

$$\Omega \begin{cases} > 1, & \text{for } k > 0, \\ = 1, & \text{for } k = 0, \\ < 1, & \text{for } k > 0. \end{cases} \tag{1.16}$$

It is now possible to connect the matter content and the geometry of the universe. This constitutes our knowledge of the universe, especially that it is flat and expanding, as well as that the expansion rate is increasing.[4] For following considerations of this thesis, however, it is particularly interesting that the matter density parameter Ω_m can be separated into further components, namely baryonic matter (Ω_{baryon}), neutrinos (Ω_ν) and dark matter (Ω_χ):

$$\Omega_m = \Omega_b + \Omega_\nu + \Omega_\chi \tag{1.17}$$

From the conclusions of various observations, these proportions can be disentangled, as will be outlined in the following section. Furthermore, it will be shown that we have good reasons to believe that, first of all, dark matter is roughly five times more abundant than ordinary baryonic matter. Secondly that Neutrinos are more or less negligible with respect to the energy density. Latest data is presented by the Planck satellite mission [11], showing 26.8 % of the energy content of the universe to be dark matter. This is five times more than the 4.9 % attributed to baryonic matter. The remaining 68.3 % and, thus, the major part of the energy density in the universe consists of so-called dark energy.

1.3 Evidence for Dark Matter

1.3.1 Velocity Distributions of Galaxies

The first compelling evidence for the existence of global dark matter was provided by F. Zwicky in 1933. Zwicky found that additional non-luminous matter is needed to explain the velocities of galaxies in the *Coma cluster* [138]. Assuming that the Coma-system is in a

[4] These paradigmatic publications are particularly noteworthy in this context: [105] [110]. The accelerated expansion is addressed by a substantial contribution of so-called dark energy and opens up a wide range of open questions within present day physics.

mechanicaly stable state, the total mass of the cluster can be estimated via the Virial theorem $\langle E_{kin} \rangle = -\frac{1}{2}\langle E_{pot} \rangle$:

$$\frac{3}{5}\frac{GM}{R} = \frac{1}{2}v^2 \tag{1.18}$$

Estimating the total mass of *Coma* by the number of observed galaxies (800) and the average mass of a galaxy (about $10^9 M_\odot$) as well es the physical size (around 10^6 ly), the potential energy of the system can be calculated and therefrom the velocity dispersion. Comparing that value to the observed average velocity dispersion along line-of-sight, one comes up with a significant discrepancy indicating dark matter. In 1937 Zwicky published another paper in which he refined and extended his analysis. Determining the ratio of gravitationally interacting to luminous matter in terms of solar mass $M_\odot$ and luminosity $L_\odot$, Zwicky found that $\frac{M}{L} \approx 500\frac{M_\odot}{L_\odot}$. Therefore, most of the matter in the galaxy cluster is dark, meaning non-luminous [138]. Similar analyses were made by Sinclair Smith in 1936, who had studied the Virgo Cluster [118].
In the following years, discourse was dominated by two questions: First, whether galaxies could be treated as mechanically stable. Second, the question of the nature of this "missing mass" within galaxy clusters, since gaseous were successively ruled out i.e. by Penzias 1961 [103] and Woolf 1967 [132].

1.3.2 Galactic Rotation Curves

In the 1970s, the dark matter paradigm became widely accepted in the physics community through a revolution of the measurement of rotation curves of stars in galaxies. Starting with the study of the Andromeda Nebula in 1970, Kent Ford and Vera Rubin decisively improved the quality of data, compared to existing measurements [111].
Only some years later there were explicit claims that additional mass was needed in the outer parts of some galaxies, when comparing the rotation curves predicted from photometry and the 21 cm hydrogen line observations.[5] The problem was that these stars did not behave as expected in a Keplerian way, which predicts that their velocities decrease with $1/\sqrt{r}$.
If one considers a star with the mass m on an orbit with the distance r to the center of its galaxy, its velocity can be calculated within classical mechanics, assuming that the cen-

[5] Photometry measures the intensity of light radiated by astronomical objects, while the 21 cm line is an especially popular hyper-fine transition of Hydrogen within radio astronomy.

tripetal force is equal to the attracting gravitational force of the mass inside its orbit:

$$|\vec{F}_z| = \frac{mv^2}{r} = \frac{GmM(r)}{r^2} = |F_g\vec{r}av| \,. \tag{1.19}$$

Solving this equation with $M(r) = 4\pi \int_0^r \rho(r')r'^2 \, dr'$ for the velocity v yields:

$$v = \sqrt{\frac{GM(r)}{r}} \quad \propto \quad \frac{1}{\sqrt{r}} \,. \tag{1.20}$$

Thus, especially for stars of the outer parts of the galaxy, where $M(r)$ is more or less the total mass of the galaxy, the velocity should decrease with $v \propto 1/\sqrt{r}$. However for an increasing number of galaxies rotation curves, the velocity did not behave that way and seemed to appear "flat" instead, [6] requiring additional non luminous matter within these galaxies. An example for this behavior is shown in figure 1.1 depicting the rotation curve of the the M33 spiral galaxy.

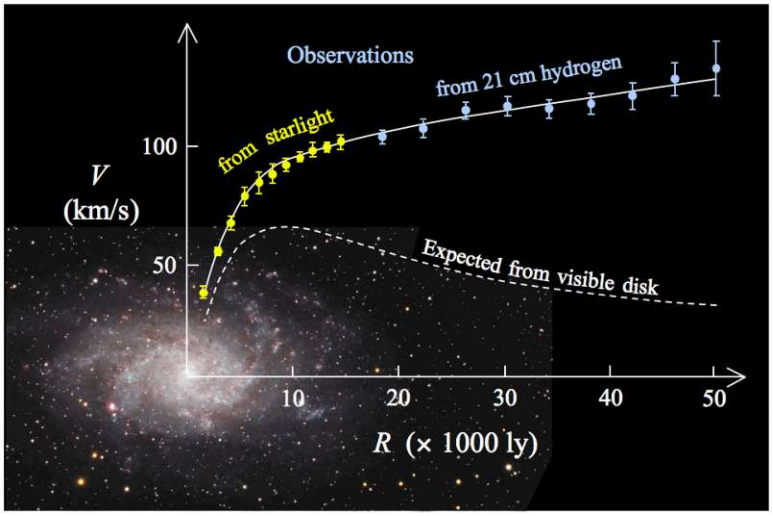

Figure 1.1: The rotation curve (velocity as a function of the distance to the center of the galaxy) of the spiral galaxy M33 (yellow and blue dots) in comparison to the Keplerian expectation from visible matter (dashed line). Including a dark matter halo gives the solid line, which is in agreement to the measured data from [50]. The illustration can be found at [46], the image in the background depicts the galaxy M33.

[6] See [40] for more comprehensive discussion of these observations.

1.3.3 Gravitational Lensing and the *Bullet Cluster*

The possibility that masses might only attract themselves due to gravity but might also deflect light is already addressed within classical physics. It is however Einstein's general theory of relativity and the concept of a curved space-time, that provides an extensive understanding of how the trajectory of light is bent when it passes massive objects. Just like an ordinary lens, distributions of matter bend the light from a distant source on its way to the observer. This bending can be understood as the consequence of a gradient in the speed of light (c) constituted by a change of the gravitational potential. In 1919, this effect famously confirmed Einstein's theory with an impressive experiment conducted by Frank Watson Dyson and Arthur Stanley Eddington during a solar eclipse. It an opportunity to measure the deflection of light from the Hyades star cluster due to the gravitational field of the sun [56]. The angle of deflection θ towards a mass M at a distance r can be expressed by:

$$\theta = \frac{4GM}{rc^2} \tag{1.21}$$

with G being the gravitational constant and c the speed of light.
Observing multiple sources of light allows to statistically deduce the strength of the gravitational lens between the light sources and the observer. The orientation of the distorted images allows to draw conclusions about the mass distribution constituting a gravitational lens. This does not only provide further evidence for dark matter. Gravitational lensing can also be used to map the distribution of all gravitationally interacting matter (luminous as well as non-luminous).

A spectacular, rather recent observation in that context was the collision of two galaxy clusters, often referred to as *Bullet Cluster*, consisting of two well separated sub-clusters [49]. Through gravitational lensing, it was found that the distribution of matter largely coincides with the individual (luminous) sub-clusters, contributing about 2 % to the total mass. With X-ray measurements, additional baryonic mass – more specifically hot gaseous clouds consisting of mostly H and He ions and contributing about 15 % of the total mass – was observed. Measurements before the collisions show, that the gaseous clouds were fairly evenly distributed around the center of mass. This changes after the collision between the two sub-clusters: a visible bow shock, more important still, a significant spacial mismatch to the mass distribution are formed in the gas. Figure 1.2 shows an overlay of three measurements of the *bullet cluster* after the collision: X-ray measurements in red and the mass distribution in blue (measured with gravitational lensing) are shown against the background of the visible spectrum, giving a comprehensive picture of the cosmological event:

Figure 1.2: Optical image of the *Bullet Cluster* (1E 0657-558) after the collision overlayed with an X-ray measurement (red) and a gravitational lensing map (blue). For details see text. From Ref. [45]

When interpenetrating each other, the stars of each sub-clusters were hardly distorted, due to the large distances between them. The gaseous clouds, on the contrary, interacted with each other and were slowed down due to friction. This seems not to be the case for the mass distribution (blue), indicating no or very little self-interaction. As a result the gas (red) appears dislocated with respect to the stars and the mass distribution (blue). This is explained by a substantial amount ($\sim$ 83 %) of non-baryonic dark matter within the mass distribution, hardly slowing down due to friction. Therefore, the *bullet cluster* does not only indicate dark matter. It also reveals properties of its self-interaction.

1.3.4 Cosmic Microwave Background

The discovery of a cosmic microwave background in 1965 by Arno Penzias and Robert Wilson [104] lead to a shift of paradigm in modern cosmology. Not only does it provide a landmark evidence of the Big Bang theory. It also had an effective influence on the discourse on dark matter.

Decoupling of matter and radiation in the early universe describes a process where particles fall out of their thermal equilibrium with each other. Before that, the production and disintegration of hydrogen were in equilibrium:

$$p + e^- \leftrightarrow H + \gamma\,. \tag{1.22}$$

This changed with the universe's gradual expansion and thus cooling. The mean photon (*gamma*) energy decreased and when it no longer reaches the threshold of the ionization energy of hydrogen of 13.6 eV, the disintegration ($H + \gamma \rightarrow p + e^-$) was no longer possible. At about 378 000 years after the Big Bang, at a temperature about 3000 K, the rate of disintegration was strongly suppressed. The resulting lack of free electrons and protons allowed the decoupling of radiation and baryonic matter. The universe changed from being an opaque plasma of charged particles into being transparent, now consisting of electrically neutral matter and radiation. Since photons were able to travel freely through space rather than constantly being scattered by charged particles, the ones produced in the final phase of production ($p + e^- \rightarrow H + \gamma$) can still be observed today. They have been red-shiftet to microwaves and, thus, designated *cosmic microwave background* (CMB).
The most precise measurement of the CMB is provided by [11], giving an almost perfect black body spectrum at a temperature of T = (2.7260 $\pm$ 0.0013) K [66]. Still, the measurements show anisotropies in an order of 10^{-5}, which can be explained by density fluctuations of the produced hydrogen during the process of decoupling. The Sachs-Wolfe-effect [113] takes account for these anisotropies: photons emitted from denser regions have to overcome a higher gravitational potential and therefore experience a red-shift. The red-shift is in direct proportion to the gravitational potential, while photons from regions below average densities appear blue-shifted. Yet, the inhomogenity of baryonic matter within the early universe cannot be understood without the presence of non-baryonic clamped dark matter. This allows, as already mentioned, to determine the various energy density parameters by precise measurements of the CMB as carried out by [11].

1.3.5 Big Bang Nucleosynthesis

The discovery of the cosmic microwave background also lead to an increased interest in Big Bang nucleosynthesis (BBN), which describes the production of first composite nuclei and light elements during cool-down of the early universe. The first composed nucleus was deuterium (1 proton + 1 neutron):

$$n + p \leftrightarrow D + \gamma \tag{1.23}$$

In a similar matter, other light elements up to ^{7}Li were created. Studying nucleosynthesis, it can be understood that the deuterium content in the universe can only build up if the disintegration drops. This is due to the expansion and associated cooling of the universe leading to a lack of photons exceeding the required binding energy of 2.2 MeV. However,

since free neutrons are unstable, the total amount of light elements in the universe – in particular the amount of ^{4}He, ^{2}H and ^{7}Li – constrains the baryon density parameter with a current value of $\Omega_b = 0.04$ [39, 4]. Since the "budget of baryons" is sensitively limited by this, everything points to the existence of a large amount of non-baryonic dark matter. The next section discusses the most promising candidates accounting for it.

1.4 Dark Matter Candidates

While the last section presented evidence for the existence of dark matter, this section gives an overview of possible models of its underlying nature. A particle nature of dark matter is assumed and it is taken into account that all the evidence of its existence is based on its gravitational interaction. This work is based on the following properties of dark matter particles, implied by the above mentioned:

a) The interaction between dark matter and baryonic matter as well as the self interaction of dark matter is weak or zero, with the exception of gravitational interaction. Among various other reasons, this is why dark matter particles neither take part in the strong interaction, nor are they electrically charged.

b) Dark matter particles move slowly compared to the speed of light (they are non-relativistic). This cold dark matter model is motivated by the *structure formation* of the early universe. It is argued that relativistic (hot) dark matter particles would have formed different structures within the universe as we observe today.

c) Dark matter is understood as non-baryonic dark matter. Although MAssive Compact Halo ObjectS (MACHOS) were considered a viable dark matter candidate, they are not addressed within this thesis. This is well motivated by the fact that the already discussed "budget of baryons" does not leave much room for MACHOS [128].

These constraints leave numerous theoretical particles which could act as dark matter in the universe. Some of them shall be discussed briefly.

1.4.1 Neutrinos

Since they are the only Standard Model particles, which are massive as well as color and electrically neutral, Neutrinos fulfil all of the above requirements, except being cold. While Standard Model Neutrinos are ruled out as an explanation for dark matter, hypothetical

massive sterile Neutrinos are considered a candidate. They are, however, conventionally considered hot dark matter, which rules them out as the single explanation for dark matter. Yet, some more recent models claim that Neutrinos could act as warm or even cold dark matter [68].

1.4.2 Axions

Although Quantum Chronodynamics (QCD) explicitly allows CP-violations in the strong interaction, such behaviour has not yet been observed. The axion was introduced to solve that so-called *strong CP-problem*. Measurements of the electric dipole moment of the neutron (EDM) provide the most stringent constraints for the CP-violating term. Axions could make up for either fractions or for the complete dark matter abundance in the universe, dependent on the particular model [83]. They can be converted to photons in strong electromagnetic fields and vice versa (Primakoff-effect), which offers a possibility for direct detection. Axions and Neutrinos give rise to exciting approaches to dark matter physics, they will, however, not be discussed in detail within the scope of this work.

1.4.3 Weakly Interacting Massive Particles (WIMPs)

Weakly Interacting Massive Particles (WIMPs) are widely favoured dark matter candidates for several reasons. In the considered standard scenario, one assumes that WIMPs were produced within the radiation-dominated period of the early universe in collisions between particles of the thermal plasma. WIMPs were constantly produced and annihilated in generic particle–antiparticle collisions:[7]

$$\chi\bar{\chi} \leftrightarrow e^+e^-, \mu^+\mu^-, q\bar{q}, W^+W^-, ZZ, HH, \dots . \tag{1.24}$$

As the universe expands, the temperature of the plasma becomes cooler, leading to an exponential decrease of the produced WIMPs while production and annihilation reactions remain in equilibrium. Since the expansion of the universe causes a decrease in the number density of particles n, the annihilation rates, which are proportional to n, also gradually decrease. This is called the freeze-out, leaving us with an abundance of WIMPs today. The relic density of WIMPs can be computed via the the WIMP number density n and the law of entropy conservation:

[7] for a more detailed discussion consider [39].

$$\frac{\mathrm{d}n}{\mathrm{d}t} = -3Hn - \langle\sigma_{ann}v\rangle(n_\chi^2 - n_{eq}^2)\,, \tag{1.25}$$

$$\frac{\mathrm{d}s}{\mathrm{d}t} = -3Hs\,. \tag{1.26}$$

Here, t is time and s is entropy density, the Hubble constant H accounts for an expanding universe, n_{eq} and n_χ are the equilibrium density and the WIMP density respectively. The average thermal WIMP annihilation cross section is depicted by $\langle\sigma_{ann}v\rangle$ [40, 124]. Inserting 1.26 in equation 1.25, inserting the Hubble constant $H^2 = \frac{8\pi}{3{M_P}^2\rho}$ and substituting $Y = \frac{n}{s}$ and $x = m/T$, with T being the photon temperature, gives:

$$\frac{\mathrm{d}Y}{\mathrm{d}x} = \frac{1}{3H}\frac{\mathrm{d}s}{\mathrm{d}x}\langle\sigma_{ann}v\rangle(Y^2 - {Y_{eq}}^2)\,. \tag{1.27}$$

The above can be solved numerically after some further adjustments. For a relic density, matching the current observed dark matter density, this leads to a particle with a mass and cross section typical for the scale of weak interaction ($\mathcal{O}(10\mathrm{GeV}/c^2)$). This astonishing alignment is often referred to as the *WIMP miracle*.
A further reason for the popularity of the WIMP is that *Supersymmetry* (SUSY) predicts the existence of a stable elementary particle with a mass less than a few TeV and having weak interactions with ordinary matter [81]. In SUSY theories, every Standard Model particle gets assigned a supersymmetric partner. The lightest supersymmetric particle could fulfill the role of the WIMP, as it needs to be stable. Should it exist, its cosmological abundance would account for a dark matter candidate.

1.5 Multiple Component Dark Matter

Multiple component dark matter models have been discussed for over a decade. They assume that the dark matter density Ω_χ is not constituted by one particle, but has multiple components. Multi-component dark matter models can arise in many different-theory scenarios. They can be realised in self-interaction dark matter models (see e.g. [99]), or supersymmetric theories (see e.g. [137]) or via enlarged $\mathbb{Z}_N$ symmetries (see e.g. [44] for a specific realization via $\mathbb{Z}_5$ symmetries). A model independent approach of the possible detectability of dual-component dark matter is given by Stefano Profumo et. al. [108], adressing *multiple* WIMP species, as well as axions and sterile neutrinos. It should be noted in particualr that multi-component dark matter scenarios present themselves via a range of dark matter masses and couplings with Standard Model particles. Should there be a dark mat-

ter component of $\mathcal{O}(100\ \mathrm{GeV})$ mass coupling to quarks, this will lead to direct detection via nuclear recoils, while components with masses $\mathcal{O}(\mathrm{GeV})$ or lighter could manifest via Bremsstrahlung or electron scattering, depending on their coupling to Standard Model particles. Multi-component dark matter scenarios thus offer a possibility of leaving various signatures at direct detection experiments. Different distribution and relic densities introduce another layer of complexity. Nevertheless, taking up multiple component theories could be an exciting path for direct detection experiments if the "classical" WIMP stays hidden. The simulation of possible interaction and detector rates constitutes critical groundwork for this approach.

Chapter 2

Detection of Dark Matter

All the indications for dark matter discussed in 1.3 affirm its gravitational interaction. A successful detection, however, would imply an additional interaction between dark matter particles and particles of the Standard Model. Since we have ruled out strong and electromagnetic interactions, most dark matter searches focus on detection through weak interaction. It was also pointed out that, if dark matter particles are too light to detect them with classical nuclear recoils since they would produce signals below threshold, only interactions with the electron shell are left for direct detection experiments.

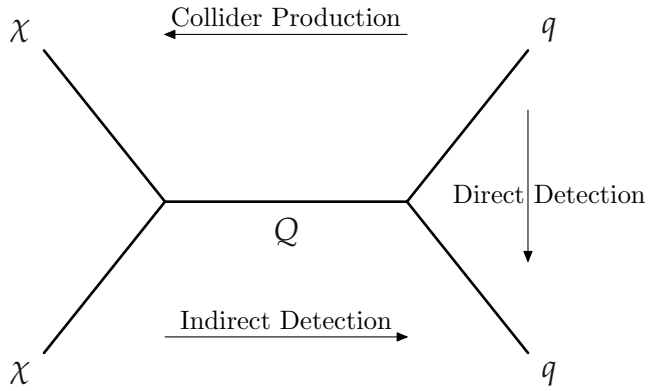

Figure 2.1: Feynman diagram indicating possible non-gravitational interactions between Standard Model particles q and dark matter χ, via one generic mediator Q. The arrows indicate possible approaches for dark matter detection.

Today's search for dark matter can be divided into three main approaches: **Indirect detection**, **searches at colliders** and **direct detection**. While indirect searches try to observe dark matter particles, e.g. at the center of galaxies, by annihilating into Standard Model particles (see section 2.1 for possible annihilation processes), collider searches try to produce

dark matter particles in collisions of Standard Model particles. This work focuses on the approach of direct detection experiments, which look for interactions of dark matter particles with Standard Model particles in earth-bound low background detectors. The Feynman diagram in figure 2.1 illustrates all three detection approaches. This chapter briefly reviews indirect detection and the search for dark matter within particle colliders, while direct detection techniques will be discussed in more detail later.

2.1 Indirect Detection

Most models of dark matter allow the annihilation of dark matter particles into pairs of Standard Model particles (e.g $\mu^+\mu^-, W^+W^-, \tau^+\tau^-, b\bar{b}$). These particles are believed to lead to the emission of cosmic rays such as $e^-, \overline{p}, \nu, \gamma$, which are aimed to be found by *indirect dark matter detection*. Most experiments focus on charged cosmic rays, gamma rays and Neutrinos.[8]

A bump in the spectrum of *charged cosmic rays* with a hard cut-off at the mass of the dark matter particle could be an indicator for dark matter, which strongly depends on the Standard Model particles produced in the annihilation process. *Gamma rays* could be produced either during the annihilation process or via virtual internal **Bremsstrahlung** [42]. These rays would result in characteristic spectra corresponding to dark matter mass. A crucial constraint in this regard is that γ-rays could also be produced in processes following the annihilation smearing out the characteristic spectrum. *Neutrinos* from the center of the sun could carry another promising signature of dark matter. If dark matter particles were captured in the gravitational potential of the sun, they would lose energy by scattering with the sun's matter and accumulate in its center, resulting in a locally enhanced rate of annihilation. Neutrinos produced in this process could reach earth-bound detectors as Super-Kamiokande [48] and Ice-Cube [4].

Indirect searches strongly relay on the dark matter density distribution within our universe, in order to sort out which regions on the sky provide the most promising circumstances for the wanted cosmic rays. Due to its high gravitational potential and, thus, high dark matter density, the galactic center constitutes a preferred region. This goes along with multiple different sources of background from multiple other sources of cosmic rays.

[8] For a detailed review of indirect dark matter search consider [67].

2.2 Production at Colliders

Detection in colliders assumes that dark matter is produced in high-energy collisions of Standard Model particles. A major constraint in that regard is that dark matter particles would not leave any electromagnetic signature in the detector and therefore would leave the detector without any signal. Hence, the only observable channel available to account for a possibly produced dark matter particle is the missing energy in the events. As an example, the depicted Feynman diagram (figure 2.2) shows the production of a dark matter particle/antiparticle pair $\chi\overline{\chi}$ and initial state radiation of a photon, within a simplified model exchanging one mediator V. This is one out of many approaches of the ATLAS [1] or CMS [47] collaboration using the LHC located at CERN. But also BELLE-II [10] at KEK and others follow similar approaches.

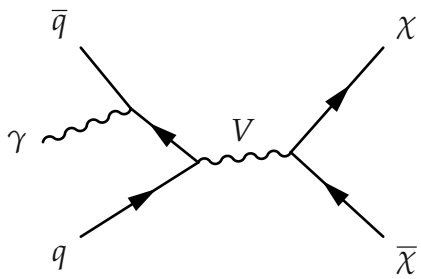

Figure 2.2: Production of pairs of dark-matter particles ($\chi\overline{\chi}$) via an explicit-channel mediator, V.

Although collider searches seem promising, they have two major limitations: Firstly, finding the signature of a dark matter particle in a collider is not sufficient proof for that particle pervading the universe. Secondly, it can not be measured whether its lifetime is long enough to fulfill the astronomical constraint (i.e. a lifetime in the range of the age of the universe). Nevertheless, finding a dark matter candidate within a collider would be a great step forward in the search for dark matter.

2.3 Direct Detection

This work focuses on the third pillar of dark matter search – *direct detection*, which aims to measure dark matter particles through their interaction with Standard Model target materials in earth-bound experiments. In this regard it is commonly expected that dark matter scatters elastically off the nucleus of the target material (**nucleus scattering**). This thesis dis-

cusses additional possible interactions with the target material, namely **electron scattering** (as discussed in e. g. [60]), the **Migdal effect** (as discussed in e.g. [78]) and **Bremsstrahlung** (as discussed in e.g. [21]). This section examines these effects as well as the anticipated recoil energy spectra by modelling a dark matter halo and interactions of the particles it consists of with a target material. All these effects are expected to give low scattering rates with rather small recoil energies. Direct detection experiments therefore demand highly sensitive detection mechanisms in a low-background environment. In this context, some experimental approaches shall be discussed as well.

It is important to keep in mind, that even if one assumes that dark matter is made of WIMPs, many questions remain unanswered. In particular, one could construct models where more than one WIMP species exist or where WIMPs interact with Standard Model quarks and leptons with significant strengths. It should be noted that existing astrophysical constraints may not be able to distinguish between single or multi-component WIMP scenarios. In this regard, understanding the experimental prospects and exploiting experimental data for a "bottom-up" model building exercise could prove useful.

This work follows such an approach by analyzing the processes of dark matter electron scattering, the Migdal effect and dark matter nucleus scattering and identifying their overlap with each other. The dark matter masses and interaction cross sections are treated as free parameters, keeping in mind that the aim is to provide input for more complex theories of dark matter through an analysis of the overlap.

It is to be noted that the analysis is carried out by assuming a single dark matter candidate and assumes that relic density is satisfied without going into details. Should there be more than one dark matter particle candidate, the corresponding rates would simply rescale according to their respective abundance.

2.3.1 Nucleus Scattering

Detection via nucleus scattering is based on the assumption of elastic and coherent scattering of dark matter particles with the nuclei of some target material. The total interaction rate with an ideal detector can be written as [73]

$$R = \frac{M_{Target}}{m_N} \cdot \frac{\rho_\chi}{m_\chi} v \cdot \sigma(v)\,. \tag{2.1}$$

This equates to a product of three main factors: The first one ($\frac{M_{Target}}{m_N}$) is the total number of nuclei in the target material. The dark matter flux penetrating the earth and, thus, the detector is given by the second factor ($\frac{\rho_\chi}{m_\chi} v$) with the local density ρ_χ and the dark matter

particle mass m_χ. Equation 2.1 assumes that all dark matter particles travel through space with same speed (v). The last factor is the interaction cross section $\sigma(v)$ for interactions of the dark matter particle with the nucleus, which generally depends on the velocity v.
Usually total rate and differential event rate in terms of counts per kg target material, keV recoil energy and days of time are of particular interest, the latter is given by [39]

$$\frac{\mathrm{d}R}{\mathrm{d}E_R} = \frac{\rho_\chi}{m_N m_\chi} \int_{v_{min}}^{v_\infty} v f(v) \frac{\mathrm{d}\sigma}{\mathrm{d}E_R}(v, E_R)\, dv \tag{2.2}$$

The dark matter-nucleus cross section generally consists of two terms: a spin-independent and a spin-dependent contribution. The spin-dependent term is coupled to the net spin of the nucleus while the spin-independent term benefits from A^2 enhancement, where A accounts for atomic mass. Due to this overall enhancement of the spin-independent cross section we focus on spin-independent scattering. Thus, the spin-dependent term is often neglected and the differential cross section can be written as

$$\frac{\mathrm{d}\sigma}{\mathrm{d}E_R} = \frac{2 m_N A^2 f^2}{\pi v^2} F^2(E_R)\,, \tag{2.3}$$

where the coupling strength (f) is assumed to be equal for protons and neutrons. $F(E_R)$ is the form factor of the nucleus and takes into account its spacial structure. The assumption of nucleus scattering allows to compute the recoil energy of the nucleus in terms of scattering angle in the center of mass frame (θ) ([40, 348])

$$E_R = \frac{{\mu_N}^2 v^2 (1 - cos(\theta))}{m_N} \qquad \mu_N = \frac{m_x m_N}{(m_\chi + m_N)} \tag{2.4}$$

where μ_N is the the dark matter-nucleus reduced mass. The maximum energy is transferred by a head on collision, i.e. $\theta = 0$, which yields ${E_R}^{max}(v) = \frac{2v^2 {\mu_N}^2}{m_N}$. This allows to rewrite equation 2.3 by defining a punctual dark matter-nucleus cross section σ_0 at zero momentum transfer [39]:

$$\frac{\mathrm{d}\sigma}{\mathrm{d}E_R} = \frac{\sigma_0}{{E_R}^{m}ax(v)} F^2(E_R) \tag{2.5}$$

The integral of some velocity distribution $f(\vec{v})$ over the velocity v takes into account that the velocities of the particles within a dark matter halo are not equitable. The lower limit of the integral, given by the minimal velocity a dark matter particle needs to have in order to

create an energy deposition E_R, can thus be expressed via equation 2.4 by

$$v_{min} = \sqrt{\frac{m_N E_R}{2\mu_N{}^2}}\,. \tag{2.6}$$

The upper limit is given by the galactic escape velocity v_{esc}, i. e. the maximum velocity of dark matter particles bound to the galaxy. The above allows to reformulate equation 2.2 to

$$\frac{\mathrm{d}R}{\mathrm{d}E_R} = \frac{\rho_\chi}{2m_\chi \mu_N{}^2}\sigma_0 F^2(E_r)\int_{v_{min}}^{v_\infty = v_{esc}} \frac{f(\vec{v})}{v}\mathrm{d}^3 v \tag{2.7}$$

Astrophysical Parameters

The astrophysical parameters are usually covered by the standard *Dark Matter Halo*. This assumes an isotropic, isothermal sphere with a local dark matter density $\rho_0 \equiv \rho(r = R_0)$, where $R_0 = (8.0 \pm 0.5)$ kpc is the solar radius (with respect to the galactic center) [39]. Within the community, a canonical local density of $\rho_0 = 0.3\ \mathrm{GeV\ cm^{-3}}$ is used.
Furthermore, an isotropic Gaussian velocity distribution often referred to as *Maxwellian* is used. It assumes no self-interaction of the dark matter particles yielding to the distribution $f(v)$, with respect to the rest frame of the galaxy. With $f(v)$ being truncated at the galactic escape velocity v_{esc}, it can be written as:

$$f(v) = \frac{1}{\mathcal{N}}\left(\frac{3}{2\pi v_{rms}^2}\right)^{\frac{3}{2}} \exp(-\frac{3v^2}{2v_{rms}^2})\theta(v - v_{esc})\,, \tag{2.8}$$

with the normalisation $\mathcal{N}$ given by:

$$\mathcal{N} = \mathrm{erf}(z) - \frac{2}{\sqrt{\pi}} z \exp(-z^2) \qquad \text{with} \qquad z := \frac{v_{esc}}{v_\odot}\,. \tag{2.9}$$

Here $v_\odot$ denotes the velocity of the sun on its trajectory around the center of the galaxy. For the dark matter halo the root mean square velocity v_{rms} is given by $v_{rms} = \sqrt{\frac{3}{2}} v_\odot$.
In order to calculate the velocity distribution in the detector's rest frame a time-dependent Galilean transformation $\vec{v} \to \tilde{\vec{v}} = \vec{v} + \vec{v}_E(t)$ has to be carried out.[9] Here, $\vec{v}_E(t) = \vec{v}_{\odot,r} + \vec{v}_{\odot,p} + \vec{v}_{Earth}$ is the earth's velocity in the galactic rest-frame, consisting of the earth's orbit around the sun ($\vec{v}_{earth}$), the peculiar motion of the sun $\vec{v}_{\odot,p}$ and the rotation of the sun around the center of the galaxy $\vec{v}_{\odot,r}$. Taking into account the tilted angle of $\gamma = 60°$ of the plane in

[9] Since cold dark matter is assumed, the halo consists only non-relativistic particles.

which the earth rotates around the sun with respect to the galactic plane and assuming a circular orbit, the absolute value $|\vec{v}_E|$ can be approximated with [114]:

$$|\vec{v}_E| = v_\odot + v_{earth} \cos(\gamma) \cos\left(\frac{2\pi}{1\text{year}}(t - t_0)\right) , \tag{2.10}$$

where $v_\odot = \vec{v}_{\odot,r} + \vec{v}_{\odot,p}$ (the peculiar motion is usually neglected). The velocity of the earth v_{earth} is about 30 km/s, the contributions of the sun $v_\odot$ canonically make up to 220 km/s. $t_0 \approx$ June 2$^{\text{nd}}$ refers to the maximum velocity of the earth in galactic coordinates. This is due to the fact that, at this time of the year, it moves in the same direction as the sun moves around the center of the galaxy. Half a year later, the earth is vis-à-vis on in its orbit, which yields the minimum relative velocity. Resulting variation of relative dark matter velocity is roughly 10 % – an annual modulation which could be measured with earth-based detectors. It shall be mentioned that real detectors aren't sensitive to the full velocity distribution, but only to velocities high enough to produce a recoil above a threshold. The modulation of a scattering rate can thus be significantly different to the annual modulation of the earth's velocity and would be measured with a distinctive period and phase. Besides this annual modulation, a diurnal modulation can be claimed because of the earth's rotation. An earth-based detector near the earth's surface experiences a variation of $\pm$450 m/s, the resulting variation of detector rates, however, is not only small compared to the annual modulation but also beyond current experimental reach [75].

Parameter		Value	
Galactic escape velocity	v_{esc}	544 km/s	[117]
Solar velocity	$v_\odot$	220 km/s	[90]
Local dark matter density	ρ_{DM}	0.3 GeV/cm^3	[90]

Table 2.1: Parameters of the standard *Dark Matter Halo* model used in this work.

Table 2.1 sums up relevant parameters used in this work. Although these parameters aren't the most recent and there already are more elaborate dark matter halo models (see e.g. [91]), these canonical models with the above parameters are still in use to ensure comparability between direct detection experiments. Broadening our knowledge of the dark matter halo will be imperative to determine properties of dark matter particles, in case of their detection in direct detection experiments.

The Form Factor

Transferred momentum from a dark matter particle to the nucleus can easily be expressed via the energy-momentum relation

$$q = \sqrt{2m_N E_R} \,. \tag{2.11}$$

Above a certain momentum transfer in a scattering event, a point-like approximation of the respective nucleus is no longer valid. Instead, its spacial structure has to be taken into account. In that regard, the form factor $F(E_R)$ as in 2.7 is introduced. For direct detection searches, the *Helm Form Factor* with the first spherical Bessel function (j_1) is used most frequently [76]:

$$F(q) = 3\frac{j_1(qr_n)}{qr_n} \exp\left(-\frac{1}{2}q^2s^2\right) , \tag{2.12}$$

where r_n is an effective nuclear radius and s is the width of the Gaussian function. The Helm-parametrization allows to analytically calculate the form factor for any nucleus of known radius r_n. In order to be independent of the nuclear radius (r_n), which is not necessarily well known, J.D.Lewin and P.F. Smith introduced an approximation from experimental scattering data [90]:

$$r_n = \sqrt{c^2 + \frac{7}{3}\pi^2a^2 - 5s^2} \,, \tag{2.13}$$

using the parameters:

$$c = 1.23 \cdot A^{\frac{1}{3}} - 0.6\text{fm} \qquad a = 0.52\text{fm} \qquad s = 0.9\text{fm} \,. \tag{2.14}$$

Another approach is a *model independent* form factor, as proposed by [55]. Experimental data from electron scattering are used to approximate the mass distribution by a sum of Bessel functions. However, experimental data are not available for all elements, which makes the Lewin/Smith approach especially convenient. This work uses model independent form factors for calcium and oxygen. Since there is no experimental data for tungsten, a Wood-Saxon approximation for the nuclear potential is used as suggested in [55]. As the calculations for nucleus scattering are based on [109], the target material $CaWO_4$ was computed with a combination of a model-independent form factor (calcium, oxygen) and a Wood-Saxon approximation (tungsten). Other target materials are computed with the Lewin-Smith method.

Nucleus Scattering in an ideal Detector

The expected differential dark matter scattering rates of $CaWO_4$ and Xenon are depicted in figure 2.3. For low recoil energies, impacts of the form factors are negligible. In this regime, the A^2-dependency of the scattering cross section is best visible. Thus, in figure 2.3 (b) tungsten dominates the spectrum because of its high mass A_W = 184 u, while A_{Ca} = 40 u and A_O = 16 u. At higher energies, the form factor causes a steep drop, best seen within the two pronounced dips of tungsten. Following the same argument xenon with an atomic mass of A_{Xe} = 131.3 u is a very suitable target material for dark matter detectors as depicted in figure 2.3 (a).

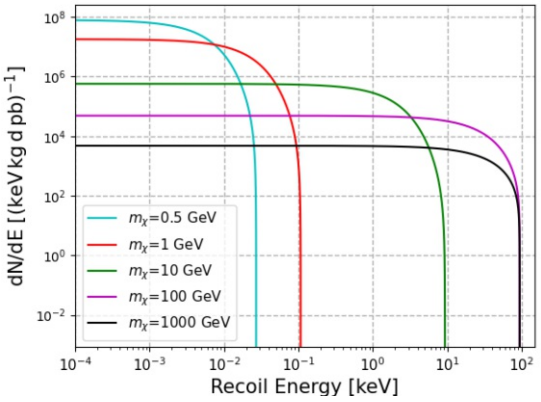

(a) Differential recoil rate of xenon for different dark matter particle masses (see legend). Note that both axes are logarithmic.

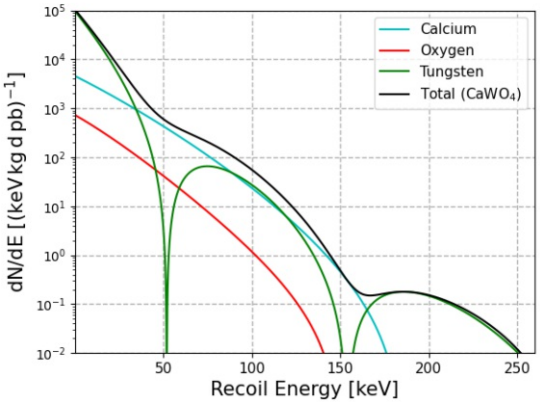

(b) Differential recoil rate of oxygen (red), calcium (cyan), tungsten (green) as well as the weighted sum $CaWO_4$ (black) as a function of recoil energy for a dark matter particle with a mass of 100 Gev/c^2.

Figure 2.3: Differential recoil rates as a function of energy for different detector materials and dark matter particle masses.

The recoil spectrum of xenon in figure 2.3 (a) shows another characteristical behavior: The curves get steeper for lower dark matter particle masses. This is caused by two things: Firstly, the expected number density of dark matter particles is inversely proportional to its mass, as the total dark matter energy density is determined by the canonical value of $\rho_{DM} = 0.3\ \mathrm{GeV/cm^3}$. In addition, the energy transferred within the scattering process decreases with a decreasing dark matter mass. Hence, composite target materials (like $CaWO_4$) have a major advantage: Light Nuclei (like oxygen) enhance the sensitivity towards lower dark matter particle masses, while heavy nuclei (like tungsten) do so towards higher masses. This allows to probe dark matter interactions simultaneously on multiple targets within one material. The energy of nuclear recoils is potentially below the lowest energy threshold

achieved in existing direct detection experiments. These, in turn, seem to be above theoretical recoil energies of low-mass dark matter particles. Consequently, elastic scattering of the nucleus does not allow detection of dark matter candidates much below the GeV mass scale. For so-called *Low-mass Dark Matter* candidates (LDM) different detection techniques are necessary.

2.4 Electron Scattering

Dark matter electron scattering is a novel approach which allows to constrain light dark matter scenarios. Dark matter electron scattering assumes that dark matter particles could also scatter inelastically on the target material. This allows dark matter particles to initiate *Electron Ionization*, *Electronic Excitation* and *Molecular Dissociation* [62]. This work concentrates on the ionization process. Since these processes wouldn't require energies higher than 1-10 eV, they could be initiated by scattering of dark matter particles with masses in a range of $\mathcal{O}(\mathrm{MeV})$. Possible signals within these processes could be electrons, photons, ions or phonons. All of them are within reach of current direct detection experiments [62].
In a similar matter as in section 2.3.1, a possible detection rate can be computed once the physical interaction between dark matter particle and target material is specified. In the following, it is assumed that dark matter interacts directly with electrons of the target material. Its interaction can be parametrized in a model-independent way, with a reference cross section σ_e and a dark-matter-form-factor $F_{\mathrm{DM}}(q)$ [62]:

$$\overline{\sigma_e} \equiv \frac{\mu_{\chi e}^2}{16\pi m_\chi^2 m_e^2} \left.\overline{|\mathcal{M}_{\chi e}(q)|^2}\right|_{q^2=\alpha^2 m_e^2} , \tag{2.15}$$

$$\overline{|\mathcal{M}_{\chi e}(q)|^2} = \left.\overline{|\mathcal{M}_{\chi e}(q)|^2}\right|_{q^2=\alpha^2 m_e^2} \times \left|F_{\mathrm{DM}}(q)\right|^2 . \tag{2.16}$$

$\overline{\sigma_e}$ is equal to the non-relativistic dark matter electron elastic scattering cross section. The momentum transfer q is fixed to the reference value αm_e. [10]

Ionization in Atoms

Considering single atoms as in liquid noble gas experiments, the dark matter–electron scattering process can be described by a S-matrix, with $\overline{|\mathcal{M}_{\chi e}(q)|^2}$ being the squared matrix element averaged over initial and summed over final spin states. Thus, a dark matter particle can scatter at an electron bound in an atomic energy level i and ionize it to an unbound

[10] This is an arbitrary value, but appropriate for atomic processes.

state with positive energy, $E_R = \frac{k'^2}{2m_e}$ (see also [37], [86]). The thermally averaged differential cross section for this interaction is given by [62]:

$$\frac{d\langle\sigma^i_{ion}v\rangle}{d\ln E_R} = \frac{\overline{\sigma}_e}{8\mu^2_{\chi e}} \int q\, dq \left|f^i_{ion}(k',q)\right|^2 \left|F_{\mathrm{DM}}(q)\right|^2 \eta(v_{\mathrm{min}}) \tag{2.17}$$

The term $\eta(v_{\mathrm{min}})$ depicts the mean inverse speed, which has the dark matter velocity distribution encoded: $\langle\frac{1}{v}\theta(v-v_{\mathrm{min}})\rangle$ (see also [114]). $f^i_{ion}(k',q)$ describes the form factor for ionization [62]:

$$\left|f^i_{ion}(k',q)\right|^2 = \frac{2k'^3}{(2\pi)^3} \sum_{\mathrm{degen.states}} \left| \int \mathrm{d}^3x \tilde{\psi}^*_{l'k'm'}(\vec{x})\psi_i(\vec{x}) \exp(i\vec{q}\vec{x}) \right|^2 . \tag{2.18}$$

The sum is over the final state angular variables l' and m' as well as over all degenerate occupied initial states. The unbound wave-functions are normalized to $\langle\tilde{\psi}_{k'l'm'}|\psi_{\tilde{klm}} = (2\pi)^3\delta_{l'l}\delta_{m'm}\frac{1}{k^2}\delta_{k'-k}\rangle$. The above allows to compute a differential event rate,

$$\frac{dR_{ion}}{d\ln E_R} = N_T \frac{\rho_\chi}{m_\chi} \frac{d\langle\sigma_{ion}v\rangle}{d\ln E_R} , \tag{2.19}$$

where N_T is the number of target nuclei per unit mass, A is the mass-number of the target material and ρ_χ is the local dark matter density. Using the astrophysical parameters exemplified in in section 2.3.1, a differential recoil spectrum can be computed in a similar matter as above.

Ionization in Crystals

The specific electron configuration within crystals, more specifically their band structure, allows to significantly lower their threshold for dark matter electron scattering and thus makes them especially attractive for low-mass dark matter regimes. In semi-conductor crystals, upon scattering with a dark matter particle, an electron is excited from a valence to a conduct band, where it could drift towards a detector. This allows to derive a scattering rate in a similar matter as above. The electrons residing in energy bands are described with Bloch wave functions $\psi_{i,\vec{k}}(\vec{x})$ [62]:

$$\psi_{i,\vec{k}}(\vec{x}) = \frac{1}{\sqrt{V}} \sum_G \psi(\vec{k}+\vec{G}) \exp(i(\vec{k}+\vec{G})\vec{x}) . \tag{2.20}$$

Here, i is the band index, $\vec{k}$ is the electron momentum in the first Brillouin Zone and $\vec{G}$ the vector in the reciprocal lattice of volume V. For an interaction that excites the electron from a valence energy band i to a conduction band i', one could express the velocity averaged cross section as [62]:

$$\langle \sigma_{cr}^{i\to i'} v \rangle = \overline{\sigma_e} \int \frac{q\mathrm{dq}}{\mu_{\chi e}^2} |F_{\mathrm{DM}}(q)|^2 \int_{\mathrm{BZ}} \frac{V\mathrm{d}^3\mathrm{k}}{(2\pi)^3} \langle \mathcal{F}_{i\to i'}^2(\vec{q},\vec{k},v_{\mathrm{min}}) \rangle \,, \tag{2.21}$$

$$\langle \mathcal{F}_{i\to i'}^2(\vec{q},\vec{k},v_{\mathrm{min}}) \rangle = \int \frac{\mathrm{d}^3 v}{v} \int \frac{d\phi_v}{2\pi} |f_{cryst}^{i\to i'}(\vec{q},\vec{k})|^2 f_{\mathrm{MB}}(\vec{v}) \theta(v - v_{\mathrm{min}}) \,, \tag{2.22}$$

$$\text{with} \quad v_{\mathrm{min}} = \frac{\Delta E_B}{q} + \frac{q}{2m_\chi} \,, \tag{2.23}$$

with f_{MB} being the Maxwell-Boltzmann velocity distribution as introduced in 2.8, ϕ_v is defined on the plane perpendicular to the direction of the incoming DM velocity v. The form factor for crystals is given by:

$$f_{cryst}^{i\to i'}(\vec{q},\vec{k}) = \sum_G \psi_{i'}^*(\vec{k}+\vec{G}+\vec{q}) \psi_i(\vec{k}+\vec{G}) \,. \tag{2.24}$$

The energy gap is given by $\Delta E_B = E_{i'}(\vec{k}+\vec{q}) - E_i(\vec{k})$. The crystal axis defines a preferred direction, hence, the scattering rate technically depends on the orientation of the crystal. This is not considered within this work, instead it is averaged over the form-factor as in [62]:

$$\langle \mathcal{F}_{i\to i'}^2(\vec{q},\vec{k},v_{\mathrm{min}}) \rangle = \int \frac{\mathrm{d}\Omega}{4\pi} |f_{i\to i'}(\vec{q},\vec{k})|^2 \eta(v_{\mathrm{min}}) \,. \tag{2.25}$$

In this work, form factors as computed by QUANTUM ESPRESSO [69] [70] were used (given at [135]). The approach uses density-functional theory to compute a local density approximations. This yields to a differential rate ([59]):

$$\frac{\mathrm{d}R_{crystal}}{\mathrm{d}\ln E_e} = \frac{\rho_\chi}{m_\chi} N_{cell} \overline{\sigma_e} \alpha \cdot \frac{m_e}{\mu_{\chi e}^2} \int \mathrm{d}\ln q \left(\frac{E_e}{q} \eta(v_{\mathrm{min}}(q,E_e)) \right) F_{DM}(q)^2 |f_{crystal}(q,E_e)|^2 \,. \tag{2.26}$$

Electron Scattering on ideal Detectors

Given the differential rate, the ideal detector response can be computed in a similar matter as in 2.3.1. The form factor for ionization described in equation 2.18 needs to be calculated for each individual electron.

In the field of liquid noble gases, this work only considers xenon due to its experimental importance. Still, similar calculations could be made for any other noble gas. For xenon,

only the ionization rates of the five outermost shells (5p, 5s and 4d, with binding energies of 12.4, 25.7, and 75.6eV, respectively) are considered relevant (see table 3.1). This builds on the work of [61, 62, 64], in which integrated form factors for the considered orbitals were numerically computed (see also [135]). Inserting this into equation 2.19 gives an electron scattering rate as a function of recoil energy shown in figure 2.4.

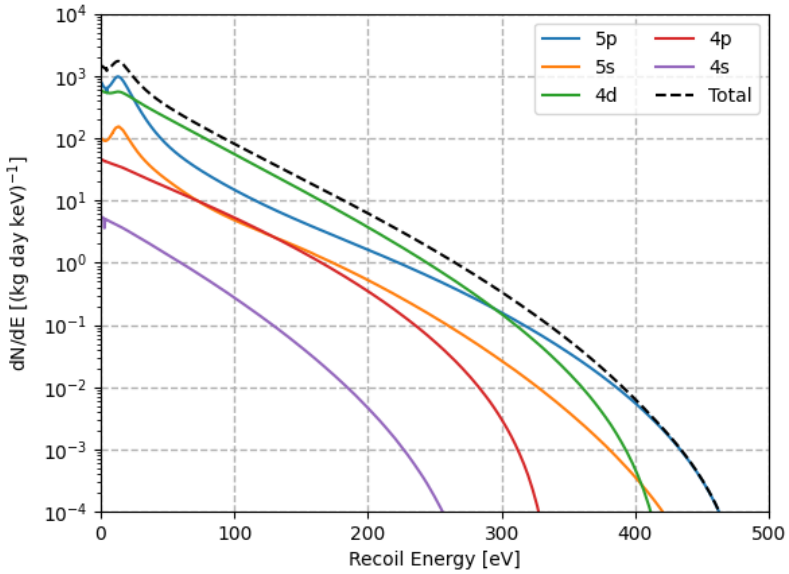

Figure 2.4: Differential electron recoil rate of xenon for a dark matter particle mass of 1 Gev/c^2. The total rate (black dashed line) is given by the sum over all orbitals. The interaction cross section is set to $\sigma_e = 10^{-36}$ cm^2.

Comparing the above figure 2.4 with the nuclear recoil spectrum depicted in figure 2.3 already points to the increased rates in the low-mass sector of dark matter electron scattering compared to dark matter nucleus scattering.
The rates derived in equation 2.26 as a function of total deposited dark matter energy E_e are shown in figure 2.5. At first glance, it can be seen that both crystals (silicon and germanium) show significantly higher rates for low dark matter masses.

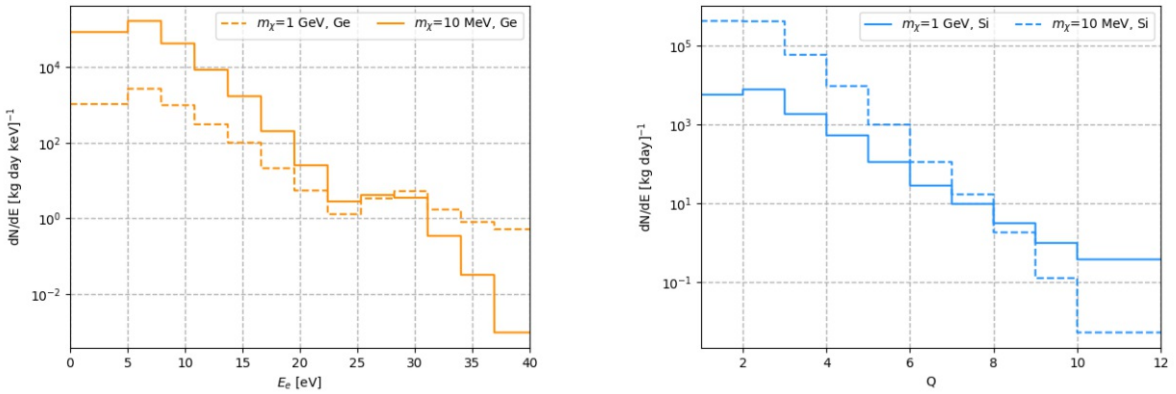

(a) Germanium (b) Silicon

Figure 2.5: Differential electron recoil spectrum as a function of ionization signal Q for dark matter particles $m_\chi = 1\,\mathrm{GeV}/c^2$ and $m_\chi = 10\,\mathrm{MeV}/c^2$ in a germanium (a) and silicon (b) target. The interaction cross section is set to $\sigma_e = 10^{-36}\,\mathrm{cm}^2$.

2.5 Migdal Effect

When a dark matter particle elastically scatters off a nucleus as described in section 2.3.1 it is assumed that the electron shells instantly follow the motion of the nucleus. This is, however, not necessarily true. It rather takes some time for the atoms' electrons to catch up, which could result in ionization and excitation of the atom. This is called the *Migdal effect*, which was first predicted by soviet physicist Arkadi Beinussowitsch Migdal [97]. It has recently been reformulated in the context of dark matter searches by Ibe Masahiro Ibe et al. [78], but also Rouven Essig, Joseph Pradler et al. [63].

While, so far, elastic scattering of the nucleus as well as elastic and inelastic scattering in the electron cloud has been discussed, the Migdal effect introduces secondary electronic recoils which accompany a nuclear recoil. The Migdal effect thus represents a three-body process, allowing a higher energy transfer than elastic scattering (two-body process). This goes along with a significantly suppressed rate. In a nutshell, the Migdal effect is a trade of rate for energy. Within liquid noble gas detectors, the Migdal effect allows to significantly lower the energy threshold, since electron recoils lose only a negligible amount of energy in form of heat compared to nuclear recoils. This is due to the small masses of electrons compared to nuclei. Following Migdal's approach, the state of an electron just after a nuclear recoil can be approximated by [78]:

$$|\Phi'_{ec}\rangle = \exp\left(-im_e \sum_i \vec{v}\hat{\mathbf{x}}_i\right) |\Phi_{ec}\rangle \tag{2.27}$$

in the rest frame of the nucleus. Here, m_e is the electron mass, $\hat{x}$ is the position operator of some i-th electron, $\vec{v}$ is the the nucleus velocity after the recoil and Φ_{ec} the quantum physical state of the whole electron cloud before nuclear recoil, with $|\Phi^*_{ec}\rangle$ denoting some ionized/excited state. The probability of ionization/excitation ($\mathcal{P}$) is given by:

$$\mathcal{P} = \left|\langle\Phi^*_{ec}|\Phi'_{ec}\rangle\right|^2 \tag{2.28}$$

Migdal's approach, however, treats the final state of ionization/excitation separately from the nuclear recoil, which leads to some obscurity within energy-momentum conversation of the process. The originality of Masahiro Ibe's et al. [78] reformulation is that the "atomic recoil cross section" is obtained coherently, which allows to derive a recoil rate as a function of recoil energy in a similar matter as above. For a detailed derivation consider [78]. The Hamiltonian of an atom can well be approximated by

$$\hat{H}_A \simeq \frac{\hat{\mathbf{p}}_N^2}{2m_N} + \hat{H}_{ec}(\hat{\mathbf{x}}_N) = \frac{\hat{\mathbf{p}}_N^2}{2m_N} + \sum_i^{N_e} \frac{\hat{\mathbf{p}}_i^2}{2m_e} + V(\hat{\mathbf{x}}_i - \hat{\mathbf{x}}_N)\ . \tag{2.29}$$

Here, $\hat{\mathbf{p}}$ and $\hat{\mathbf{x}}$ denote the momentum and the position operators. The Hamiltonian of the electron cloud $\hat{H}_{ec}$ depends on the position operator of the nucleus $\hat{\mathbf{x}}_N$ via the interaction potential $V(\hat{\mathbf{x}}_i - \hat{\mathbf{x}}_N)$. The Schrodinger equation can then be written as:

$$\frac{\hat{\mathbf{p}}_N^2}{2m_N} + \hat{H}_{ec}(\hat{\mathbf{x}}_N)\Psi_E(\vec{x},\{x\}) = E_A\Psi_E(\vec{x},\{x\})\ , \tag{2.30}$$

where the positions (including spinor indices) of N_e electrons are represented by $\{x\}$, collectively. Solving this equation gives the Eigenstates of the atom. By applying a Galilean transformation, the Eigenstates of an atom in motion can be calculated as well. These allow to calculate the differential cross section, which turns out to be [78]:

$$\frac{\mathrm{d}\sigma}{\mathrm{d}E_R} \simeq \sum_{E^F_{ec}} \frac{1}{32\pi}\frac{m_A}{\mu_N^2 v_\chi^2}\frac{|F_A(q_A^2)|^2|\mathcal{M}(q_A^2)|^2}{(m_A+m_\chi)^2}|Z_{FI}(q_e)|^2 = \frac{1}{2}\frac{m_A}{\mu_N^2 v_\chi^2}\tilde{\sigma}_N(q_N)|Z_{FI}(q_e)|^2 \tag{2.31}$$

Here, F_A is the nuclear form factor, $\mathcal{M}$ the invariant amplitude for nucleus scattering and q_A describes the momentum transfer to the atom. The Migdal factor Z_{FI} appears in the interaction term between dark matter and the nucleus, if the interactive potential is defined

in dependence of the position operator of the nucleus as shown above. The sum is carried out over the final states of the electron cloud. The last equality defines

$$\tilde{\sigma}_N(q_N) = \frac{1}{16\pi} \frac{|F_A(q_A^2)|^2 |\mathcal{M}(q_A^2)|^2}{(m_A + m_\chi)^2} \,. \tag{2.32}$$

Following the same argument as above this can be used to derive a corresponding rate:

$$\frac{\mathrm{d}R}{\mathrm{d}E_R} = \frac{1}{m_A} \frac{\rho_\chi}{m_\chi} \frac{\mathrm{d}\sigma}{\mathrm{d}E_R} \int_{v_{min}}^{v_\infty = v_{esc}} \vec{v} f(\vec{v}) \mathrm{d}^3 v = \sum_{E_{ec}^F} \frac{1}{2} \frac{\rho_\chi}{m_\chi} \frac{1}{\mu_N^2} \sigma_N(\tilde{q}_A) \cdot |Z_{FI}(q_e)|^2 \cdot \int_{v_{min}}^{v_\infty = v_{esc}} \frac{f(\vec{v})}{\vec{v}} \mathrm{d}^3 v \,. \tag{2.33}$$

As above, ρ_χ denotes the local dark matter density and $f(v)$ the dark matter velocity distribution. The above considerations are based on a scenario of dark matter particles scattering on single, isolated atoms. This is a valid approximation for the inner shells of liquid noble gas targets. Of these, xenon shall be closer examined.

2.5.1 The Migdal Effect on an Ideal Detector

Applying the above considerations on the xenon atom allows to plot theoretical detection rates as a function of energy. Starting point for this calculation is the transition probabilities published by [78], as depicted in figure 2.6 (a). Taking into account the astrophysical parameters, one can compute the theoretical rates as shown in figure 2.6 (b). As one can see, the Migdal effect allows to significantly improve the sensitivity for low-mass dark matter. The resulting rate is considered to be the sum of the contribution of each individual orbital. Yet, inner electrons ($n < 2$) are often considered to be too strongly bound to the nucleus to contribute significantly, while valence electrons ($n = 5$) are sometimes neglected as they are subdominant in the region of interest of the Xenon experiment (see [21]).

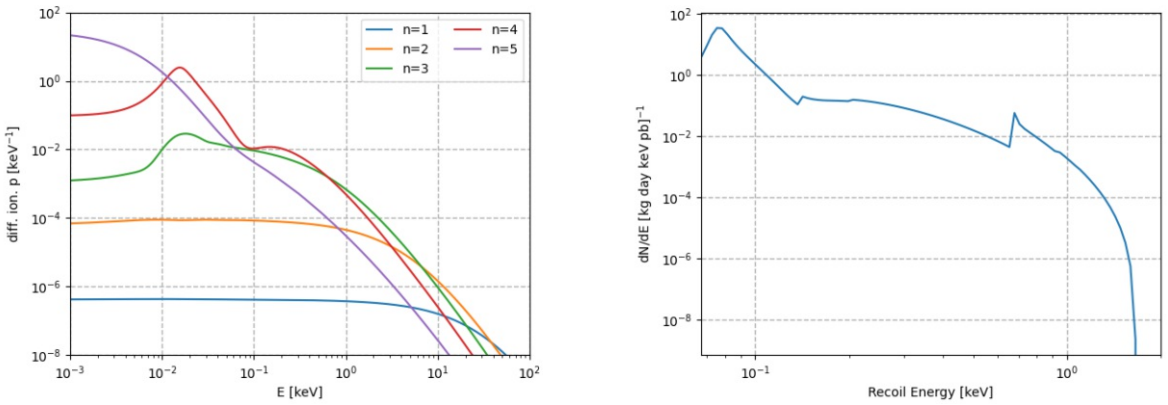

(a) Differential ionization probabilities as a function of the emitted electron energy E for isolated xenon as computed by [78]. For n=1 to n=5 all possible, final states are assumed.

(b) The ionization spectrum caused by the Migdal effect of xenon as a function of recoil energy. The dark matter mass is fixed to $m_\chi = 1$ Gev/c^2, the interaction cross section to $\sigma = 10^{-36}$ cm^2

Figure 2.6: Theoretical differential ionization probabilities as well as the resulting rates as a function of energy caused by the Migdal effect. Note that the resulting rate (especially for low recoil energies) is dependent on considered orbitals. Often, n=5 is not considered (see e.g. [21]).

2.6 Direct Detection Experiments

This chapter is concluded with a brief overview of current state-of-the-art dark matter search experiments, exploiting the outlined physical interactions. Due to the low anticipated dark matter scattering rates, one of the main challenges for all direct detection experiments is to reduce background. Shielding against cosmic rays is mostly realized by placing the experiments in deep underground sites. I addition, most experiments have both passive and active layers of shielding in order to suppress possible remaining cosmic radiation as well as environmental backgrounds. All materials used within the experiment have to be radio-pure to be suited for this kind of research.

The signals of solid state experiments reach from heat (phonons, e.g. Ge, Si, $CaWO_4$) to ionization (Ge, Si) to scintillation light ($CaWO_4$, NaI). Liquid noble gas (Xe, Ar) experiments measure scintillation light signals as well as ionization signals. Besides these experimental techniques, CCDs and superheated liquids constitute promising strategies for direct detection of dark matter.

This section focuses on the technology relevant for further considerations of this thesis, namely direct detection with liquid xenon as well as cryogenic detectors using semi-conductor crystals (Ge, Si) as target materials. Since the starting point of the considerations in this work is situated within the CRESST collaboration, this experiment is also briefly outlined. A com-

prehensive review of the state-of-the-art direct detection techniques is given by L. Baudis and S. Profumo in the current *Review of Particle Physics* [124].

2.6.1 Liquid Noble Gas Experiments

Spanning a wide range of masses, liquid noble gas experiments report the best exclusion limits over several experimental generations, the most recent being DarkSide-20k (currently under construction) [3], LUX [17], PandaX-II [51], DEAP [13], XMASS-1 [7] and Xenon1T [29]). Even though not all of these experiments are based on liquid noble gases, they share the concept of a dual phase time projection chamber (TPC), as depicted in figure 2.7. The majority of the TPC is filled with liquid noble gas, leaving some space for a gaseous layer on top. When a particle interacts with the liquid noble gas, scintillation and ionization occur. Due to the specific angle of this work, all further considerations are focused on the Xenon experiment in particular, though most of it also holds true for experiments using argon. The prompt scintillation light is measured with photo multiplier tubes (PMTs) at top and bottom of the TPC. This is called primary scintillation light or **S1-Signal**. The photo multipliers form an array, allowing reconstruction of the interaction position in the xy-plane, with the z-axis being the rotational axis of the cylindrical TPC. In addition, an electric field that causes free charges to drift from the spot where the ionization took place to the surface of the the TPC, is applied. When they enter the gaseous phase, they generate scintillation light proportional to the the charge, which is then detected by the PMTs (secondary scintillation light or **S2-Signal**). The time difference between the S1 and S2 signal allows to conclude the z-position. Since recoils on electrons induce more charge than nuclear recoils of the same deposited energy, these two can be discriminated by the ratio S2/S1. This allows for background events to be filtered out. The 3D-position reconstruction (provided by the arrangement of the PMTs and the time difference of S1 and S2-Signal) allows a fiducialization – a rejection of events taking place close to the wall of the TPC. Background suppression is very efficient here, since most backgrounds originate from outside of the TPC or its walls. Intrinsic backgrounds in the liquid phase are tackled by continuous purification [22]. The combination of purification, fiducialization and discrimination, complemented with the possibility to accumulate very large target masses, allows especially low backgrounds on comparatively high possible exposures. This is why they currently provide the best exclusion limits for "high" dark matter masses.

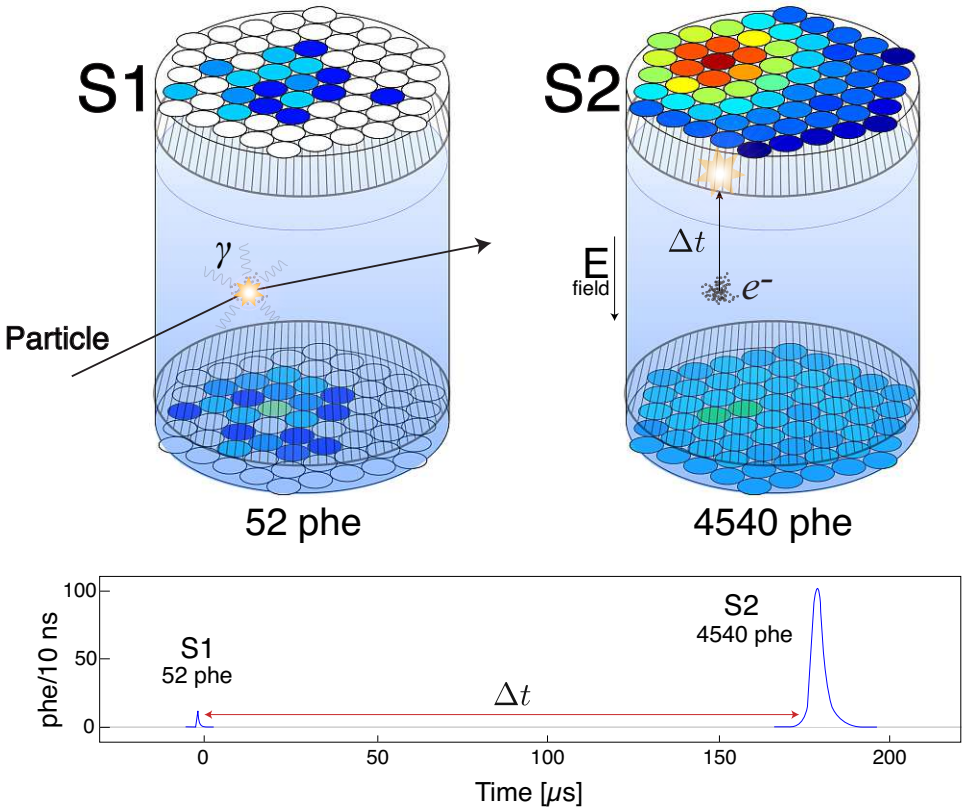

Figure 2.7: Schematic illustration of a double phase time projection chamber (TPC). The PMTs on the top and the bottom, arranged in an array, measure the primary scintillation light first, called the S1-Signal. By applying an electric field, the induced ionization products drift to the gaseous phase on top. This initiates further scintillation, called the S2-Signal, which is measured with some delay. The time difference between the two signals and the layout of the PMTs allows a 3D reconstruction of the interaction's location, allowing to use the target's self-shielding effect (fiducialization). Furthermore, the ratio of S1 and S2 allows to discriminate the particle interactions. The Illustration is taken from [96], the values of the number of photo electrons (phe) correspond to the LUX detector.

2.6.2 Experiments with Solid-State Targets

Germanium detectors are used in a variety of applications for dark matter detection by either measuring ionization (CDEX [95], TEXONO [131]), or by measuring heat, respectively phonons and ionization (EDELWEISS-III [31], CDMS [15], SuperCDMS SNOLAB [16]). The advantage of germanium detectors is their very low level of intrinsic background, which is a unique selling-point among solid state materials. CDEX and TEXONO use p-type detectors made of germanium, with masses of several hundred grams. A particle interaction

creates electron-hole pairs, drifting to a punctiform electrode by an applied electrical field. Fiducialization is made possible by potential latencies of the ionization signal. Still, it does not allow for particle discrimination. Since PPCs have very low noise levels, they provide low energy thresholds $\mathcal{O} < (1\ \text{keV})$. Other advantages of PPCs are, that they do not need mK-temperatures but are able to be operated at temperatures between 63 K and 77 K (liquid nitrogen temperatures) and that they exhibit very good long-term stability.

Cryogenic Detectors

The defining property of cryogenic particle detectors is their very low operating temperature, which typically is in the range of $\mathcal{O}(10\ \text{mK})$. These temperatures do not only reduce thermal noise tremendously, they also go along with material properties – in particular heat capacity (C) and electrical resistivity (ρ) – being especially sensitive to deposited energy. This allows to apply the bolometric technique to the search for dark matter: The energy deposition of some dark matter particle within the target material results in measurable (phonon) signals.
EDELWEISS, CDMS and (Super)CDMS SNOLAB, but also CRESST, belong to the group of cryogenic detectors in the contemporary search for dark matter, operating at temperatures between $\approx$ 50 mK and $\approx$ 20 mK. The extraordinarily low operating temperature enables detection of very small temperature changes $\mathcal{O} < (1\,\mu\text{K})$ (phonons) induced by particle interactions. Cryogenic detectors are optimized for low-mass dark matter, being able to probe masses down to $\sim$ 0.2 GeV. Via a weak electric field, the induced ionization is measured within detectors based on semiconductor crystals. In a similar matter as in liquid noble gas experiments (which is dominated by gamma and beta radiation, inducing mainly electron-hole pairs), background can be discriminated via the ionization yield, which is defined as the ratio of ionization signal to phonon signal. An ingenious arrangement of the electric field (such as the interleaved Z-sensitive Ionization Phonon (iZIP) detector used by SuperCDMS) results in an additional possible discrimination between surface near and bulk interactions. EDELWEISS uses a similar design.
Additionally, CDMS and EDELWEISS are able to amplify the phonon signal by applying a high bias voltage ($V_b \approx 70$ V) using the *Neganov-Luke effect* (see CDMSlite [14]). In doing so, the work of the drifting electron-hole pair is added to the initial phonon signal:

$$E_{total} = E_{phonon} + N_{eh} e V_b \quad . \tag{2.34}$$

The number of electron-hole pairs N_{eh} depends on the type of the initial recoil. Thus, the phonon signal effectively becomes an amplified measurement of the initially induced ionization. This improves the signal-to-noise ratio and the energy threshold, but it prevents particle discrimination. Furthermore, the CDMS collaboration uses silicon, which provides a better sensitivity for low-mass dark matter as germanium due to kinematic reasons, as an additional detector material [16].
In the search for dark matter semiconductors can be used in th shape of PPC detectors as well as cryogenic detectors, the latter being by far more complex and requiring a far larger technological effort to be stably operated. Nevertheless, this has proved its worth in terms of fiducialization and particle discrimination and makes cryogenic detectors (CDMS and EDELWEISS) the most sensitive semiconductor detectors for a wide range of WIMP masses. A major constraint for germanium and silicon based experiments is that the crystals they use hardly ever exceed a few hundred grams. This means that large target masses require many detectors and are therefore more challenging to scale up as liquid noble gas experiments.

The CRESST Experiment

The CRESST experiment uses scintillating $CaWO_4$ crystals as its target material at cryogenic temperatures, resulting in two separate detection channels: energy deposition through heat (phonons) and scintillation light [98]. In a similar fashion as in semiconductor experiments, particle interaction can be discriminated via the light yield defined as the ration of energy measured as scintillation light to energy measured in phonons: $\text{LightYield} = \frac{E_l}{E_p}$. In order to measure the extraordinarily small temperature changes induced by some particle interaction within the target material, transition edge sensors (TES) are used. These consist of a small tungsten layer evaporated onto the target substrate. This layer is superconductive for temperatures below $\sim \mathcal{O}(15\ \text{mK})$ and undergoes the transition to normal conduction within $\mathcal{O}(1-2\ \text{mK})$. Since the transition-function of resistance as a function of temperature is quite steep, small temperature changes (as induced by some particle interaction) of $\Delta T = \mathcal{O}(10\ \mu\text{K})$ lead to measurable changes in resistance $\Delta R = \mathcal{O}(10\ \text{m}\Omega)$. The temperature change through phonons can be approximated as:

$$\Delta T = \frac{\Delta E}{C}\,, \tag{2.35}$$

with the heat capacity C. For dielectric materials, such as $CaWO_4$, C scales with the third power of the temperature:

$$C \sim \left(\frac{T}{\Theta_D}\right)^3 \tag{2.36}$$

Even though this approach is oversimplified, it provides reasoning for the extraordinarily low operation temperatures of ~ 10 mK.
The scintillation light is detected through a silicon-on-sapphire (SOS) absorber. The deposited energy due to absorption of light can be read out by another TES.

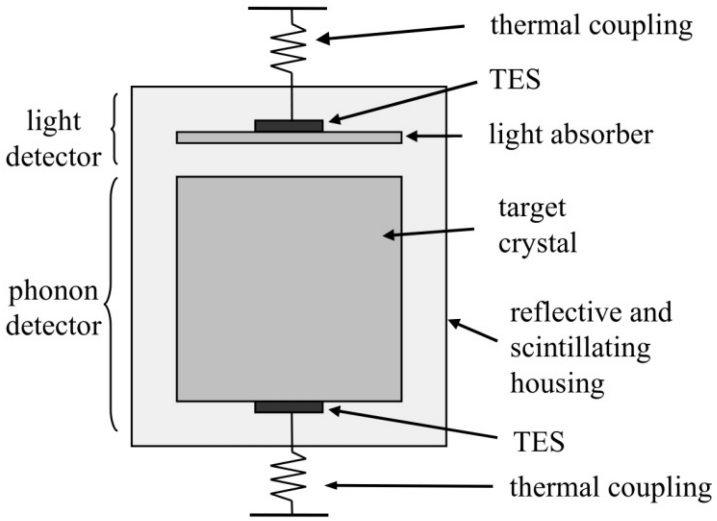

Figure 2.8: Schematic drawing of a CRESST-II detector module, consisting of a $CaWO_4$ target crystal and an independent light detector. The phonon signal induced by some particle interaction in the target crystal is measured with the TES (black). Emitted scintillation light is guided to the light detector with a scintillating and reflective foil surrounding the crystal, to be absorbed in the silicon-on-sapphire absorber, with a TES measuring induced energy. Both TESs are thermally coupled with the heat bath of the cryostat in order to cool down to operating temperature after a particle interaction. The Illustration is taken from [20].

Room Temperature Ionization Detectors

A more recent technical development in the field uses silicon charge-coupled devices (CCDs) for low-mass dark matter searches in the eV-mass range. CCDs are photo sensitive chips and have a wide commercial use, mainly in digital cameras. The particle interaction within one pixel creates electron-hole pairs drifting to electrodes at top and bottom of the pixel. Such

ionization events induced in bulk silicon of high-resistivity CCDs have charge resolutions around 1-2 e^{-1}. Just like within a digital camera, charge is accumulated at the electrodes until readout after the exposure time. The interaction's depth can be reconstructed by the signal's height in neighbouring pixels. For deeper interactions, more charge carriers will diffuse to adjacent pixels. The shape and depth of the pixel-clusters allows to discriminate background. Due to their very low energy threshold ($\sim$ 0.5 keV for nuclear recoils), CCDs present an interesting new field in the search for low-mass dark matter.
The DAMIC experiments [34] and [88] use CCDs optimized for near-infrared measurements in telescopes. SENSEI achieves single-electron sensitivity, employing the skipper technology demonstrated in [127]. A first run at Fermilab has yielded direct-detection constraints on dark matter electron scattering for masses between 500 keV and 5 MeV [9]. The DANAE project located at the Viennese Institute of High Energy Physics (HEPHY) has introduced depleted P-channel field effect transistors (DEPFET) with a repetitive non destructive readout (RNDR). Such DEPFET-RNDR detectors are very promising for future low-mass dark matter searches [85], [115].

Chapter 3

Analysis Method

This chapter lays out the analysis carried out on the experiments presented in section 2.6, keeping in mind discussed physical interactions presented in 2.3, namely**nucleus scattering** (as within the classical WIMP paradigm), **electron scattering** and the **Migdal effect**. In It aims to show the potential of new theory effects on the sensitivity of current direct-detection experiments, as well as potential energy overlaps in predicted rates. In this regard, the underlying question is to what extent dark matter nuclear and electron scattering are complementary and how one could account for this, when both of these initial particle interactions are measured in the same detection channels.
In order to answer these questions, the analysis constituting this work follows a rather intuitive approach: The starting points for consideration are the rate equations discussed in section 2.3. These rate-expressions assume an ideal detector with zero threshold and infinite energy resolution. They do not account for any secondary or tertiary reaction resulting from initial energy deposition, as discussed in section 3.1.2. Irrespective of all these, the primary observation is that – putting background aside – experiments assume only a single source of energy deposit in the detector at a given time. It is important to keep in mind that, even if dark matter could interact with Standard Model particles in different ways, within direct detection experiments there are only one or two channels to determine the interaction. This circumstance becomes especially relevant when considering that **electron scattering** and the **Migdal effect** produce an initial ionisation signal, while nucleus scattering produces heat or scintillation signals. New possible interactions therefore raise new questions concerning background discrimination and potential blind spots of direct detection experiments. To shed light on these issues, the analysis includes a calculation of the signal expectation of a real detector. The rate equations derived in section 2.3 already include information of the **dark matter halo**, the **form factors** and **electronic configurations** of the presented target materials. Nevertheless, these idealized spectra neglect operating principles of the individual experiments and their performance, in particular their secondary particle interaction,

energy thresholds and energy resolution. This section gives an overview of the further steps which have to be carried out to calculate the spectrum as each detector would *see* it, starting from the spectra of idealized detectors. The analysis differs slightly for each experiment and initial physical interaction but overall includes the following steps:

a) Implement the standard dark matter **halo model**.

b) Implement different **detector materials**, their nuclear **form factors** (for nucleus scattering) and their **Ionization form factors** or outgoing electron wave functions (for electron scattering).

c) Calculate the energy spectrum for an ideal detector, with respect to the **physical interactions** described in section 2.3.

d) Implement **conversion mechanisms** within different target materials (secondary ionization, scintillation, heat)

e) Consider detector thresholds and efficiencies, as well as their finite energy resolution.

f) Compare **estimated rates** as a function of deposited energy.

A more detailed presentation of the individual steps in relation to the individual physical interactions is shown in Figure 3.1. The following chapter discusses the presented steps and their implementations in detail. The calculations focus on the Xenon- and to some extend on the CRESST Experiment. This is mainly due to the availability of data and the work of previous groups that have studied dark matter electron scattering and the Migdal effect on xenon. As in section 2.3 each effect will be treated separately. This, however, follows rather illustrative purposes. It is important to keep in mind, that experiments are only able to *see* the excess of events at a certain energy against a certain background. But, as shown in chapter 4 up to this point they are not able to distinguish between interactions depositing the same energy into the same detection channel. This circumstance is particularly important because the discussed physical interactions, especially nucleus scattering and electron scattering, could be contradictory and, above all, there is still no empirical basis that prefers a certain interaction of dark matter with standard model matter over another.

The calculations presented are carried out in python. The assumptions on the dark matter halo are presented in section 2.3.1. Following the landscape sketched in figure 3.1, the analysis is presented according to the corresponding physical effects.

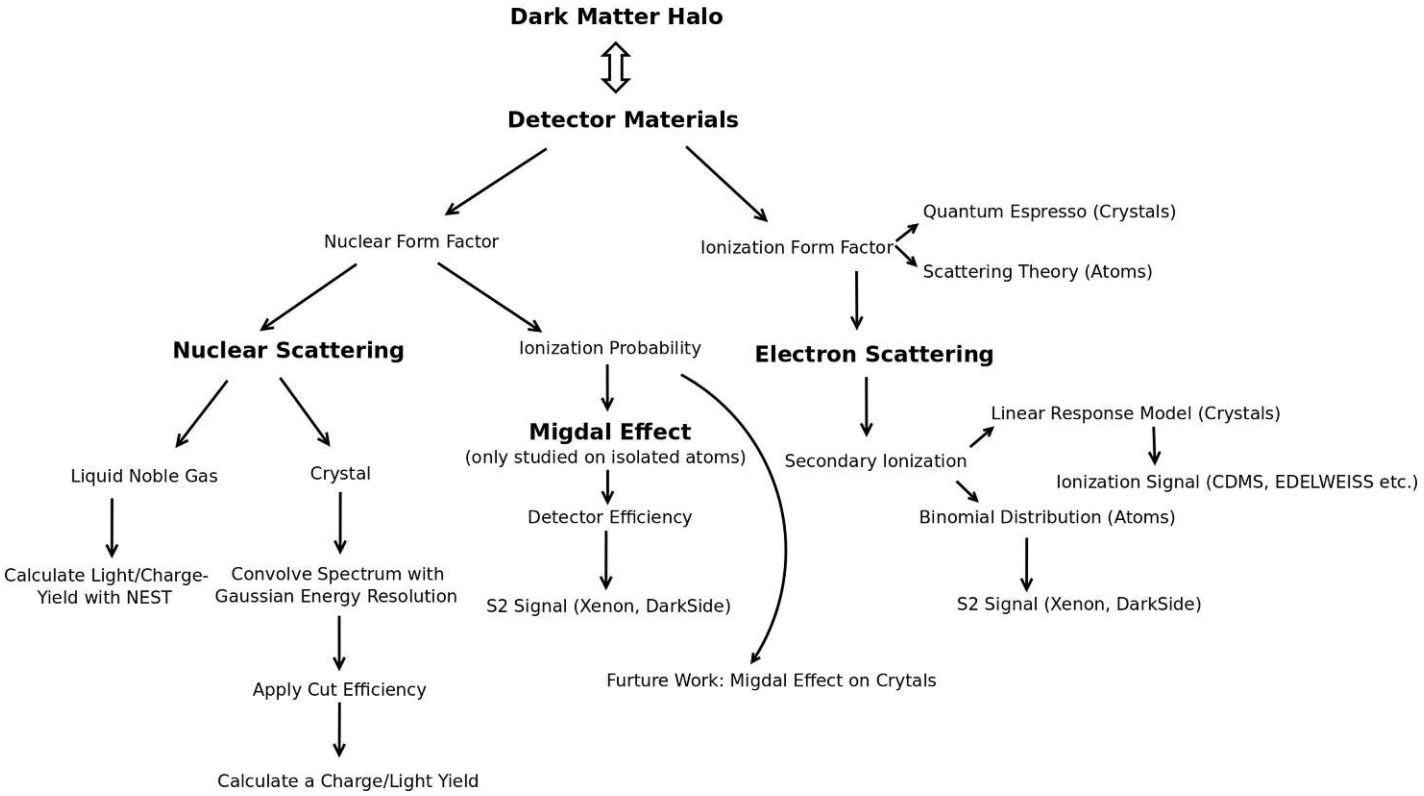

Figure 3.1: Schematic representation of the analysis carried out, based on the interaction of a dark matter halo with a detector material, distinguished according to the three physical effects discussed and their further processing.

3.1 Nucleus Scattering

The calculation of an ideal detector spectrum for nucleus scattering is described in 2.3.1. A dark matter flux penetrating the earth can be defined through the astrophysical parameters of the dark matter halo. The spacial structure of the nucleus of the detector material is accounted for by the nuclear form factor as described in section 2.3.1, to finally end up with the predicted dark matter scattering rate for an ideal detector as in equation 2.7.

3.1.1 Nucleus Scattering in Crystals

Incorporating Finite Energy Resolution

If deposited energy is measured with a phonon detector, as it is in cryogenic detectors, their finite energy resolution needs to be considered. This is dominated by Gaussian noise and therefore carried out by a convolution of the differential recoil rate $\frac{\mathrm{d}N(E_R)}{\mathrm{d}E_R}$ with a Gaussian function $g(E_R)$:

$$\left[\frac{\mathrm{d}N}{\mathrm{d}E_R} * g\right](E_R) = \int_0^{E_R} \frac{\mathrm{d}N(\epsilon)}{\mathrm{d}E_R} \cdot g(E_R - \epsilon)\mathrm{d}\epsilon \tag{3.1}$$

If the expected spectrum is binned, the integral simplifies to a summation. With an adaptive bin-size (small bins for low energies and a steep rise in events growing proportional to rising energy), to maintain a reasonable accuracy with an acceptable computation time.

Cut Efficiency/Trigger Threshold

All experiments have a certain energy-dependent efficiency function, usually resembling a blurry step function reaching full efficiency at a certain energy threshold. Additionally, to simulate the energy reconstruction of the acquired data, one needs to apply a certain cut efficiency or cut survival probability. Without going into further detail, this leads to further corrections, respectively a step-like cut-off at the energy threshold as well as multiplication factors taking into account the cut survival probability that accounts for the loss of signal events from applied data selection criteria. The data processing often also includes acceptance regions, which then also need to be considered.

3.1.2 Nucleus Scattering in Liquid Noble Gas

The starting point is, again, the rate equation derived in section 2.3.1. For the following remarks, it is useful to keep in mind the image of a Time Projection Chamber (TPC) as depicted in figure 2.7). Any particle depositing energy in a liquid noble gas[11] creates excitation of electrons and/or ionization, as well as heat (as depicted in figure 3.2). While the initial excitation leads to scintillation light (primary scintillation, S1), ionization produces free electrons which either recombine or escape. The recombination leads to excimers contributing to the scintillation light, with an almost identical spectrum as is generated by primary excitation (S1-Signal). Escape electrons are harnessed via an electric field. Their number is determined by a charge amplifier coupled to the anode in a one phase detector. In two-phase detectors, as discussed previously, these electrons produce more scintillation light, with the respective latency, in the higher-electric-field gas phase (S2-Signal). This section will give a brief overview of the scintillation model used within this work, which is based on the NEST (Noble Element Simulation Technique) analysis [122]. For a more elaborate account consider [121] and [123]. The current dark matter data analysis within the **Xenon experiment** as well as their background model's statistical inference is laid out here [25].

[11] These considerations are mostly relevant for xenon, yet, many aspects are true for other liquid noble gases.

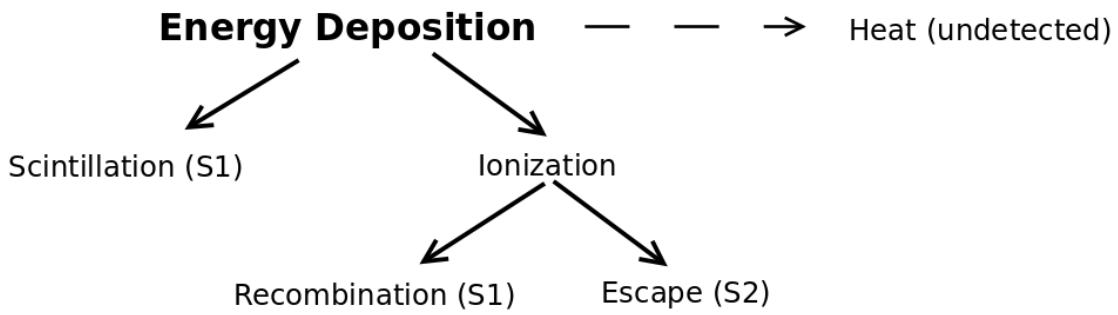

Figure 3.2: Schematics of interactions occurring after an energy deposition by any recoiling species in a noble element. See text for further details.

Since the ratio of S2 to S1 light differs for electron recoils and nuclear recoils it is the crucial parameter for particle discrimination within xenon. It is important to understand how free electrons behave after ionization. The S1 and S2 light yields are anti-correlated, since those electrons which recombine are not able to escape, while escaping electrons can not recombine (see also [121]). The recombination probability, and thus scintillation yield, is given by energy loss per unit of path length $\frac{dE}{dx}$ and the applied electric field [53]. The energy partition can be expressed with a simplified Platzmann equation [23]:

$$E_{dep} = N_{ex}W_{ex} + N_iW_i = N_i(\alpha W_{ex} + W_i)\ , \quad \alpha \equiv \frac{N_{ex}}{N_i}\ , \tag{3.2}$$

where E_{dep} is the energy deposited by a particle in a single interaction, N_{ex} is the number of excitons created per deposition, N_i the number of ions and W_{ex} and W_i the required energy to excite or ionize atoms. This leads directly to numbers of produced quanta:

$$N_i = \frac{E_{dep}}{\alpha W_{ex} + W_i} \quad \text{and} \quad N_{ex} = \alpha N_i\ , \tag{3.3}$$

which then in turn lead to N_{ph} photons and N_e ionization electrons [121]:

$$N_{ph} = N_{ex} + rN_i \quad \text{and} \quad N_e = N_i(1-r)\ , \tag{3.4}$$

where r is the recombination probability. For rather long particle tracks, r can be derived from Birks' Law [101] [52]:

$$r = \frac{A\frac{dE}{dx}}{1 + B\frac{dE}{dx}} + C\ , \quad C = 1 - \frac{A}{B} \tag{3.5}$$

The first term describes the recombination of the wandering electron through the medium, while the second term C represents the so called Onsager recombination. For short particle tracks the Thomas-Imel box model is better suited [119].The recombination probability r takes the form of [119] [125]:

$$r = 1 - \frac{\ln(1+\xi)}{\xi}, \quad \xi \equiv \frac{N_i \alpha'}{4a^2 v}, \tag{3.6}$$

where α' is a constant factor accounting for the electron-hole-pair mobility, v is the mean ionization electron velocity and a is the length scale defining the ionization density volume. Short tracks are defined as particle tracks shorter than the mean electron thermalization distance of 4.6 μm in liquid xenon.
NEST integrates the Thomas-Imel-box approach as well as the Doke's approach via Birk's law to get a unified picture of the scintillation yield for the whole energy spectrum and their corresponding particle tracks [121]. The choice of free Parameters (A, B, C) is made according to empirical data. The transition between the Thomas-Imel and the Doke regime is done with a cross-over distance at length scale of the thermalization length of the electron. This enables NEST to reproduce light yields across the whole energy spectrum of liquid noble gas detectors in accordance to empirical data.

With an increasing electric field, free electron-hole pairs are increasingly less likely to recombine with an ion. This effect is known as *electric field scintillation quenching* [24], involving several scintillation loss mechanisms, above all the *Lindhard effect* [94] [119]. This leads to an increase of S2 light at the expense of S1. Since recombination probability does not change uniformly across the energy spectrum, this problem needs to be addressed semi-empirically. NEST adapts the free parameters A, B and C within equation 3.5 and the Thomas-Imel parameter ξ / N_i in equation 3.6 with respect to the strength of the electric field.
Finally the effect of *nuclear recoil quenching* needs to be addressed, incorporating the fact that, for a given energy deposition, nuclear recoils produce less ionization than electron recoils and that much of the ionization of nuclear recoils is suppressed through recombination. This is approached by modifying equation 3.2 as follows [119]:

$$E_{dep} \cdot L(E_{dep}) = (N_{ex} + N_i)W = (1+\alpha)N_i W, \tag{3.7}$$

where L is the *effective Lindhard factor*, which needs to be determined empirically.
Figure 3.3 shows the result of the above considerations: A charge and light yield spectrum for nuclear recoil with a deposited energy between 200 eV and 100 keV. It becomes apparent that light and charge yield are anti-correlated. Thus, so is the recombination and escape of

ionized electron-hole-pairs.

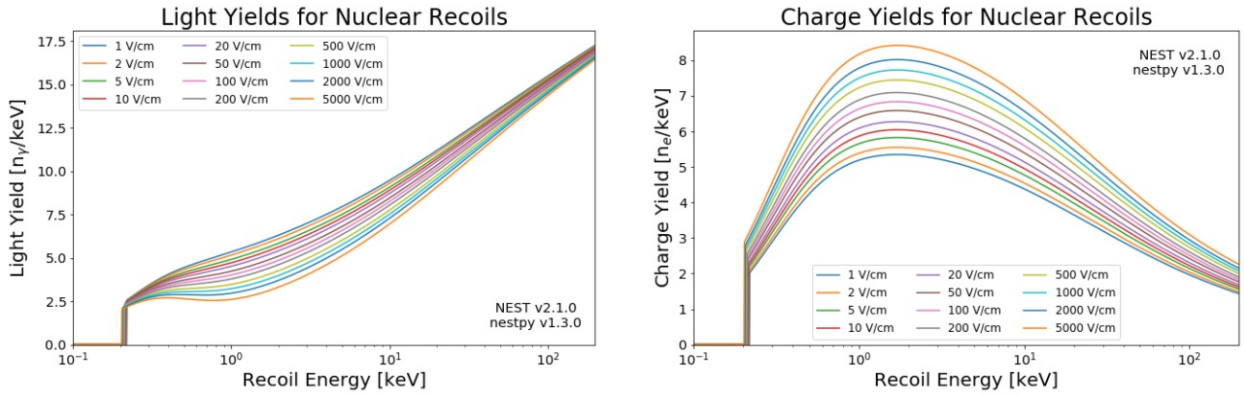

(a) Charge yield for nuclear recoils within liquid xenon.

(b) Charge yield for nuclear recoils within liquid xenon.

Figure 3.3: Benchmark Plots of light yields and charge yields for nuclear recoils computed by NEST v2.1.0. Each line represents an energy dependent yield for a certain electric field as described in the legend. Graphics taken from [100].

The light and charge yields for γ-electron recoils are given in figure 3.4. Besides the striking anti-correlation of light and charge, a higher efficiency of electron recoils, caused by the quenching effect of nuclear recoils, can be observed. Most of their energy (up to $\sim 80\%$) is transferred into atomic motion and therefore lost to heat [119]. The graphics presented also allow us to directly infer the possibility of particle discrimination.

The conversion from the particular scintillation light yield to the signal within the PMTs is simple, but characteristic for each experiment. This goes along with a certain trigger threshold which needs to be applied as discussed in section 3.1.1. As a reminder, the detector actually measures photo electrons of the PMTs which measure primary and secondary scintillation, expressed here as light and charge yield (see section 2.6.1). As can be seen when comparing figure 3.3 and figure 3.4 the ratio of charge to light yield allows to discriminate the type of interaction at a given initial energy deposition. However, this circumstance also already points to the fact that potential dark matter candidates are harder to detect as soon as other interactions besides nuclear recoils are introduced. This is especially true for interactions which deposit energy in the electron shell, like dark matter electron scattering, or induce ionization via the Migdal effect.

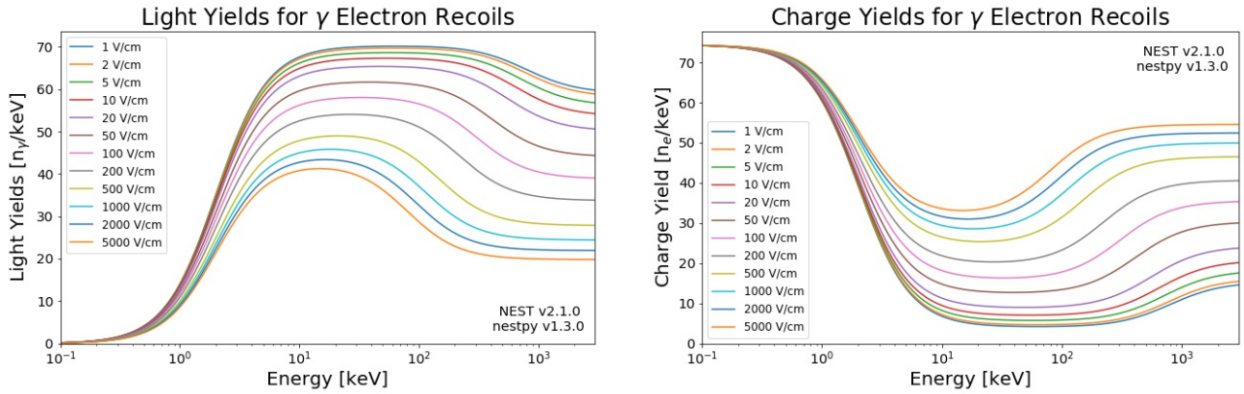

(a) Light yield for electron recoils with γ-quanta in liquid xenon.

(b) Charge yield for electron recoils with γ-quanta in liquid xenon.

Figure 3.4: Benchmark plots of light yields and charge yields for electron recoils with γ-quanta computed by NEST v2.1.0. Each line represents an energy dependent yield for a certain electric field as described in the legend. Graphics taken from [100].

3.2 Electron Scattering

3.2.1 Electron Scattering in Liquid Noble Gases

As discussed before, there are several theories suggesting that dark matter interacts with the electron shells of the matter constituting the target materials of direct detection experiments. Possible rates of an ideal detector are derived in section 2.4. As described above, an energy deposition in the electron shell of the atoms of some liquid noble gas also leads to heat, ionization and/or scintillation. This work focuses on the ionization signal, as does the current discourse on dark matter electron scattering. Following [60], the spectrum presented in figure 2.4 can be conversed to electron or charge yield n_e, using the same framework as above. The basic assumption is, that the recoiling electron ionizes and excites other atoms, producing $n^{(1)} = \text{Floor}(E_{er}/W)$ *additional* "primary quanta", being either electrons (n_e) which could be detected or undetectable scintillation photons (n_γ)[12] and heat. The additional electrons n_e are calculated with a probabilistic model based on our understanding of higher-energy electron recoils: The energy of the primary electron creates a a number of ions (N_i), and a number of excited atoms (N_{ex}), whose ratio is about $N_{ex}/N_i \approx 0.2$ for energies above 1 keV [30]. As in [60], recombination between electrons and ions is described with a modified Thomas-Imel recombination model [119], suggesting that the fraction of ions that recombine

[12]This scintillation due to recombination is only undetectable if the energies are as low as in the considered low-mass dark matter scenario. In other cases, they are very much detectable but especially hard to trace.

(f_R) is about zero at low energies resulting in $n_e = N_i$ and $n_\gamma = N_{ex}$, leading to the of initial quanta observed as electrons, f_e, given by $f_e = (1 - f_R)(1 + N_{ex}/N_i)^{-1} \approx 0.83$ [119]. The total number of quanta (n) at higher energies is observed to behave as $n = E_{er}/W$, with E_{er}, being the outgoing energy of the initial electron, and $W = 13.8$ eV, being the energy required to create a single quantum [116]. This leads to the fiducial values $N_{ex}/N_i = 0.2$, $f_R = 0$ and $W = 13.8$, used in this work as used in [60].
In addition to the quanta created via the primary electron $n^{(1)} = \text{Floor}(E_{er}/W)$, where $\text{Floor}(x)$ rounds x to the nearest smaller integer, it is assumed that the photon associated with the de-excitation is able to photoionize additional quanta $n^{(2)}$ as listed in table 3.1. The total number of detected quanta (electrons) accumulates to $n_e = n'_e + n''_e$, where n_e represents the primary electron (1 with a probability f_R, or 0 with a probability $1 - f_R$) and n''_e the secondary quanta, following a binomial distribution with $n^{(1)} + n^{(2)}$ trials and a success probability of f_e [60]. Approximating the excited electrons using the outlined procedure allows a reasonable conversion from theoretical dark matter recoil energies to a measurable ionization signal in the S2 channel of liquid noble gas experiments. It introduces, however, another source of theoretical uncertainty, like the NEST calculation.

Shell	5p	5s	4d	4p	4s
Binding Energy [eV]	12.4	25.7	75.6	163.5	213.8
Additional Quanta	0	0	4	6	3

Table 3.1: The outermost shells, binding energies as well as considered additional charge carriers during an ionization process of xenon found to be relevant for ionization through dark matter [60].

3.2.2 Electron Scattering in Semi-Conductors

The conversion from total deposited energy to an ionization signal within crystals is a similarly complicated chain scattering process as in atoms. Within this work it is approximated with a linear response model, as suggested by [59]. This model assumes that the primary electron-hole pair produced by the initial dark matter scattering initiates the production of an *additional* electron hole pair for every extra ε of deposited energy, where ε is the mean energy per electron-hole pair as measured in high energy recoils. The ionization Q is then given by [59]:

$$Q(E_e) = 1 + \text{Floor}\left(\frac{E_e - E_{gap}}{\epsilon}\right) \quad , \tag{3.8}$$

where ε and E_{gap} are measured by [120] [84] to be:

	Silicon	Germanium
ε [eV]	3.6	2.9
E_{gap} [eV]	1.11	0.67

This, admittedly very simplistic, approach is well reasoned for in [59]. For the purpose of this work, it is important to mention that it is a conservative calculation. Primarily, because it does not account for any kind of fluctuations that could push a low-energy event above the ionization threshold. This not only means that semiconductor crystals have a much lower threshold than liquid noble gases, but also that the scattering process converting the initial deposited energy into a measurable signal is much easier to approximate within crystals. This could allow a reduction of theoretical uncertainty. The resulting spectrum as a function of charge carriers is given in figure 3.5.

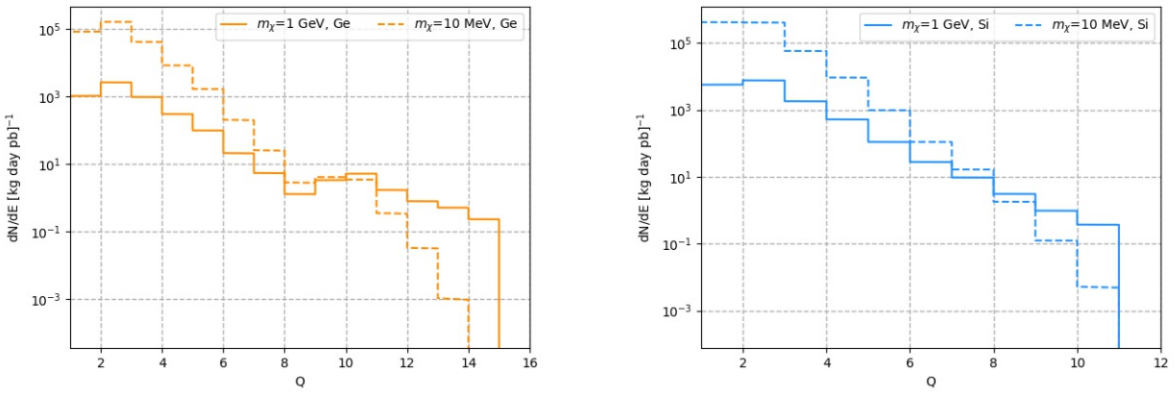

(a) Germanium (b) Silicon

Figure 3.5: Spectrum of events as function of the ionization signal Q for dark matter particles $m_\chi = 1\ \mathrm{GeV}/c^2$ and $m_\chi = 10\ \mathrm{MeV}/c^2$ in a germanium (a) and silicon (b) target. The interaction cross section is fixed to $\sigma_e = 10^{-36}\mathrm{cm}^2$.

3.3 Migdal Effect

The ideal detector rate for dark matter particles interacting with target material (in the scope of this work only xenon is discussed) via the Migdal effect is derived in section 2.5.1.[13]

[13]For the calculation of the spectrum of an ideal detector, please refer, again, to [78] and [2].

Figure 3.6 illustrates one more time, how the Migdal effect describes energy deposition in the nucleus of an atom resulting in the emission of one or more ionization electrons. Once the Migdal effect brings forth a free electron, the detector response can be treated as in 3.2, i.e. under the assumption, that the ionization electron propagates through the medium exciting and ionizing other atoms leading to $n^{(1)} = \text{Floor}(E_{er}/W)$ *additional* quanta.

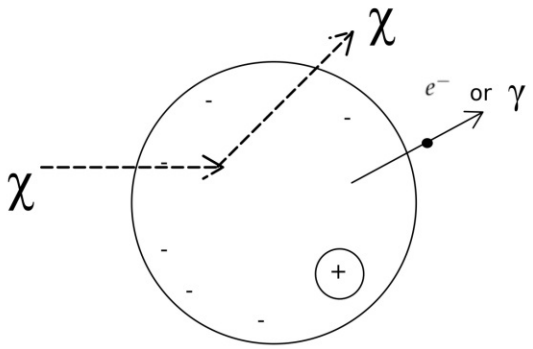

Figure 3.6: Illustration of the Migdal effect in an isolated atom.

The analysis in this work uses the same probabilistic approach for secondary ionization as in section 3.2 to simulate the detector response with the parameters given in table 3.1. This parallel treatment appears to be valid, especially because of the similar energy regime of the primary electron-hole-pairs. The cut-efficiency is also equivalent to the one of electron scattering.

Chapter 4

Results

The results presented in this chapter concern the comparability of anticipated detector signals under the assumption that none of the described interaction is preferable to another and that the interaction cross sections for nucleus scattering and electron scattering are independent. More precisely, the cross section for nucleus scattering and Migdal-mediated nucleus scattering are interdependent, explicitly being independent of the cross section for electron scattering. If one allows the dark matter halo to be constituted out of multiple different constituents (i.e. a *multi component dark matter model*), this circumstance becomes a substantial argument. There is a variety of multi-component dark matter models, which have substantial theoretical foundations (some of them are pointed out in section 1.5). There are good reasons to assume that the constituents of the dark halo could vary in:

a) their mass

b) their interaction with Standard Model particles.

First, the idealized anticipated rates in a detector for the effects and materials discussed are presented. Then, scenarios in which all three effects are visible within a single detector are emphasized in a further step. Given the additional degrees of freedom of a multiple component dark matter model, this leads to the question, whether current direct detection experiments would be able to distinguish different components of the dark matter halo. In order to make the effects comparable these rates are converted to functions of the initial response of the target material, more specifically its ionization. This results in histograms which show the differential event rate for a corresponding number of initial electrons. This kind of analysis is based on known properties of the target materials. A comprehensive analysis on all effects was only carried out within xenon, due to the availability of its form-factor for ionization as well as its ionization probability due to the Migdal effect. The idealized detector rates as a function of recoil energy have already been presented earlier in this work. The

following section shows the detector rates of each individual effect calculated as described in chapter 3.

4.1 Intrinsic Signal Response in Liquid Xenon

These calculations result in the anticipated intrinsic signal response spectra in liquid xenon, depicted in figure 4.1 for dark matter electron scattering and the Migdal effect and in figure 4.2 for "classical" nucleus scattering. The interaction cross sections are normalized to $\sigma_e = \overline{\sigma_n} = 1$ pb $= 10^{-36}$ cm^2 in case of dark matter electron scattering and the Migdal effect and to $\sigma_n = 10^{-43}$ cm^2 for dark matter nucleon scattering.[14]

The rate is directly proportional to the interaction cross section σ_i, which is most likely different for each physical interaction (although interdependent for "classical" nucleus scattering and the Migdal effect). Yet, changing the cross section merely shifts the depicted spectra along the y-axis. As a result, a change of the interaction cross section within one or more of the physical interactions described could intensify or dampen the regimes of potential overlaps in the energy and ionization spectra. This means that, if one allows multiple components of dark matter, any superposition of the calculated spectra, no matter how small (in terms of rate), is possibly relevant for further considerations, given a similar recoil energy or a similar initial ionization or scintillation response. In other words: The rate for each individual effect could be higher (or lower) as in the one depicted in the presented plots since the cross section is a priori unknown. It is therefore not necessarily valid to neglect certain effects for certain mass regions. In particular, the common practice to neglect dark matter electron scattering and the Migdal effect for higher mass regimes and nucleus scattering for lower ones is only valid for single component dark matter models. The aforementioned overlaps are studied in closer detail in the next section. Both, the overlaps in the energy and the ionization spectrum, are presented, the conversion follows the calculation presented in chapter 3.

[14] The value $\sigma_n = 10^{-43}$ cm^2 for nucleus scattering is based on current exclusion limits, the value $\sigma_e = 10^{-36}$ cm^2 lays on the upper limit of the of current constraints for popular benchmark models for DM-electron scattering, the value $\overline{\sigma_n} = 10^{-36}$ cm^2 for the Migdal effect lies within the boundaries of commonly used interaction cross sections (see e.g. [21]). It is set to $\overline{\sigma_n} = 10^{-36}$ for the sake of comparability.

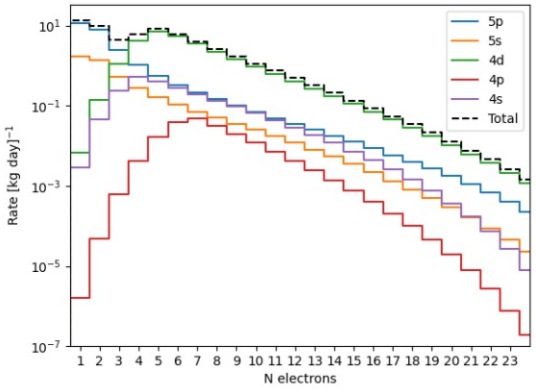

(a) Spectrum of dark matter electron scattering with a dark matter particle mass $m_\chi = 1\ \mathrm{GeV}/c^2$ and an exposure of 1 kg day per correspondent orbital (see legend) as a function of electrons. The total rate equals to the sum of the individual orbitals.

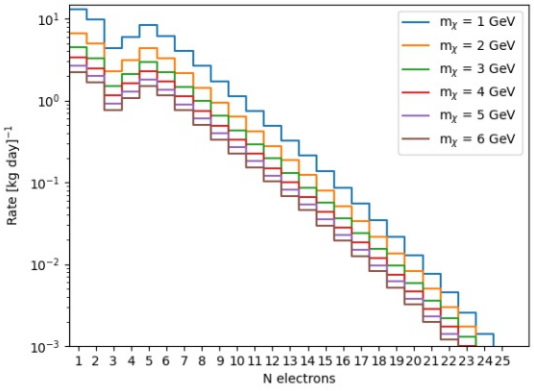

(b) Histogram of the spectrum of dark matter electron scattering (total rates) for dark matter masses $m_\chi = 1\ \mathrm{GeV}/c^2$ to $m_\chi = 6\ \mathrm{GeV}/c^2$.

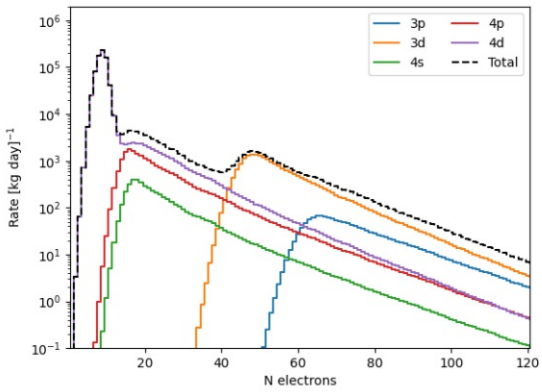

(c) Rate of ionization due to the Migdal effect for a dark matter particle $m_\chi = 1\ \mathrm{GeV}/c^2$ and an exposure of 1 kg day. Consider the legend for each corresponding orbital. The total rate equals to the sum of the individual orbitals.

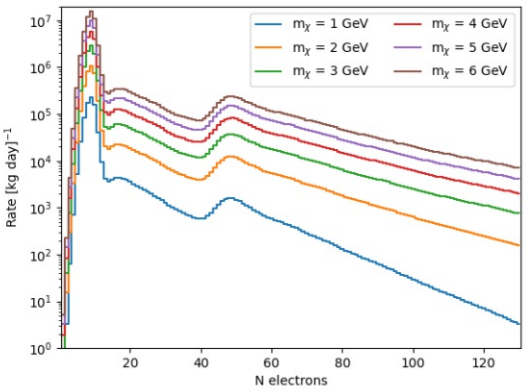

(d) Histogram of the differential rate spectrum (total rates) due to the Migdal effect for dark matter masses $m_\chi = 1\ \mathrm{GeV}/c^2$ to $m_\chi = 6\ \mathrm{GeV}/c^2$.

Figure 4.1: Histogram of the spectrum of dark matter electron scattering in (a) and (b) as well as the Migdal effect in (c) and (d), all for various xenon electron shells and dark matter masses. The spectra are calculated with the secondary ionization model described in section 3.2. The cross sections are fixed to $\sigma_e = \overline{\sigma_n} = 10^{-36}\ \mathrm{cm}^2$.

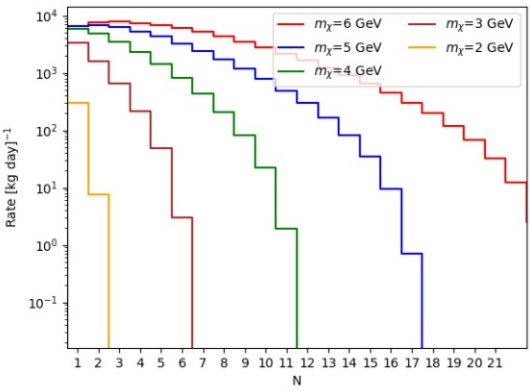

(a) The ionization signal of dark matter nucleus scattering for dark matter particle masses $m_\chi = 2$ GeV/c^2 to $m_\chi = 6$ GeV/c^2 and an exposure of 1 kg day.

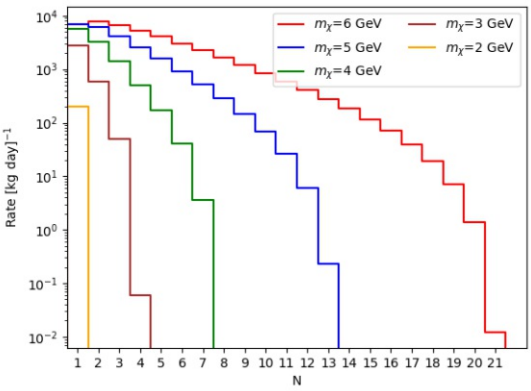

(b) The scintillation signal of dark matter nucleus scattering for a dark matter particle masses $m_\chi = 2$ GeV/c^2 to $m_\chi = 6$ GeV/c^2 and an exposure of 1 kg day.

Figure 4.2: Histogram of the differential rates per corresponding number of ionized electrons (a) and produced photons (b). The spectra are calculated with the secondary ionization model of NEST described in section 3.2. The cross section is fixed to $\overline{\sigma_n} = 10^{-43}$ cm^2.

4.2 Ionization Overlaps

Figure 4.1 shows that, for a given dark matter particle mass of $m_\chi = 1$ GeV, the whole dark matter electron scattering spectrum is overlaid by the Migdal effect. This is especially remarkable for a small window of masses below 1 GeV, since the dark matter electron scattering rate is inversely proportional to the dark matter mass – which is visible in figure 4.1 (b). [15] This overlap fades for higher masses, as shown in figures 4.3 and 4.4. One can see that for a broad variety of interaction cross sections and dark matter masses the end point of the Migdal effect is at higher energies than the dark matter electron scattering. It is also worth noting that, if the interaction cross sections are comparable, the Migdal effect is the dominant effect over the whole energy/ionization spectrum. The distinctive, step-like threshold in the ionization rate due to the Migdal effect is dependent on the considered orbitals. This work follows current discussions (see e.g. [21]) and neglects orbitals with $n = 5$, as discussed in section 2.5.1.[16]

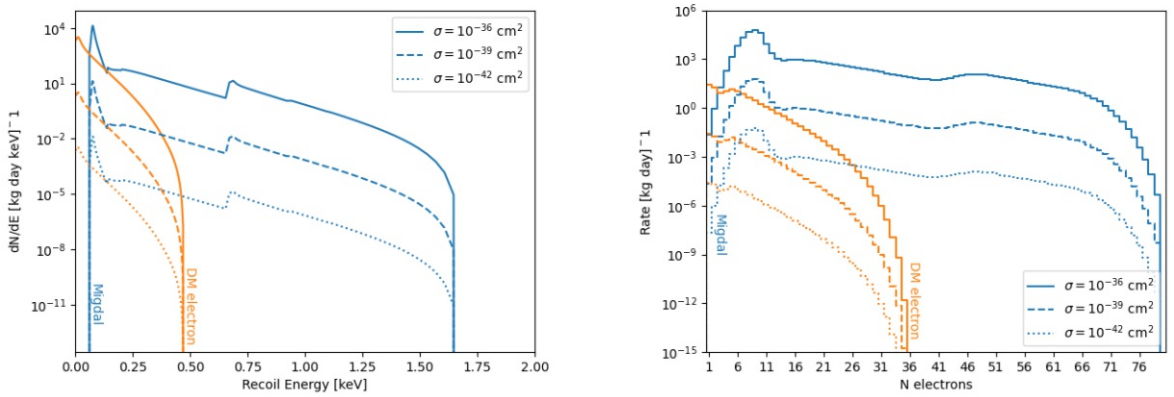

(a) DM-electron scattering rate (orange) and Migdal effect (blue) as a function of energy.

(b) DM-electron scattering rate (orange) and Migdal effect (blue) as a function of ionization electrons.

Figure 4.3: The overlap of dark matter electron scattering rate (orange) and the ionization rate due to the Migdal effect (blue) as a function of energy (a) and a function of ionization electrons (b). The dark matter mass is fixed to $m_\chi = 0.5$ GeV/c^2, while the cross section is varied from $\sigma = 10^{-36}$ cm^2 to $\sigma = 10^{-42}$ cm^2. The overlap extends across the entire DM-electron scattering spectrum (see text).

Regarding these extensive overlaps, it has to be kept in mind, that the energy deposition

[15] The rate due to the Migdal effect, on the other hand, is proportional to the dark matter mass (see figure 4.1 (d).)

[16] Even though this choice seems to be arbitrary, adding the orbitals with $n = 5$ would only raise the rates for energies < 0.05 keV, which would not change the qualitative conclusions of this section.

in the detector is very different for each physical effect. While dark matter electron scattering excites individual electrons or directly creates ionization electrons, the Migdal effect describes an excitation or ionization due to internal effects within the atom after a scattering event with the nucleus.
Figure 4.3 shows the impact of the dark matter – Standard Model interaction cross section for dark matter electron scattering and the Migdal effect respectively. The scattering rate and resulting ionization are plotted in the two figures, while the dark matter mass is fixed. As discussed before, the interaction cross section adjusts the normalization of rates. For a fixed dark matter mass, however, the end point of the spectra remains unchanged. The second feature is that, even if the rates for dark matter electron scattering and the Migdal effect are comparable, the resulting ionization signals at the detector are very different. This means that, on an average, dark matter electron scattering leads to "weaker" observable signals over Migdal effect for the same dark matter mass and scattering cross section. In other words: If one wishes to have comparable dark matter electron scattering- and Migdal effect signals, dark matter particles must couple to quarks and electrons with different strengths.
Furthermore, it is interesting to consider the effect of variation of dark matter masses on differential rates and ionization signals. This is shown in figure 4.4 for dark matter masses varying from 0.1 to 1 GeV, while keeping the cross section fixed. It can be seen that the end point of dark matter electron scattering differential rate changes by smaller amounts compared to the Migdal effect when the dark matter mass is varied over the range of interest. The resulting ionization signal is always smaller for dark matter electron scattering compared to the Migdal effect, irrespective of the dark matter mass. We conclude, that it will be easier to obtain a large overlap between dark matter electron scattering and the Migdal effect by constructing dark matter models where a dark matter particle scatters off electrons with much stronger coupling compared to the nuclear counterparts (i.e. nucleus scattering and the Migdal effect), which, in turn, will increase the ionization signal.

Assuming that we need a strong hierarchy between cross sections to obtain comparable rates, in figure 4.5, dark matter electron scattering-, Migdal effect- and dark matter nucleus scattering rates for two different dark matter masses are shown in order to observe such hierarchies between dark matter nucleus scattering, the Migdal effect and dark matter electron scattering cross sections. Corresponding ionization rates are also depicted. These figures show, in principle, that one could simultaneously obtain comparable rates if underlying dark matter models have sufficiently different cross sections for each individual effect.

If the dark matter mass is increased any further, both signals are overcome with elastic nucleus scattering signals as the dominant effect. The corresponding ionization and scintil-

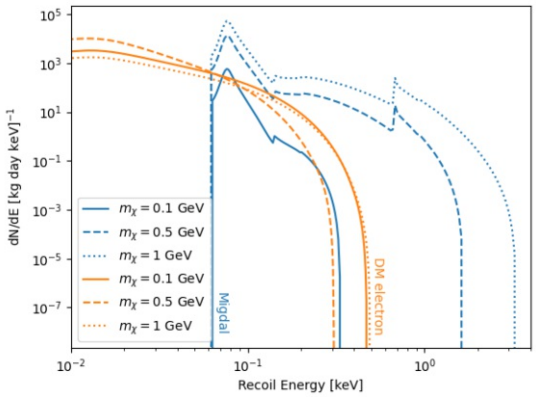

(a) DM-electron scattering (orange) and Migdal effect (blue) as a function of energy.

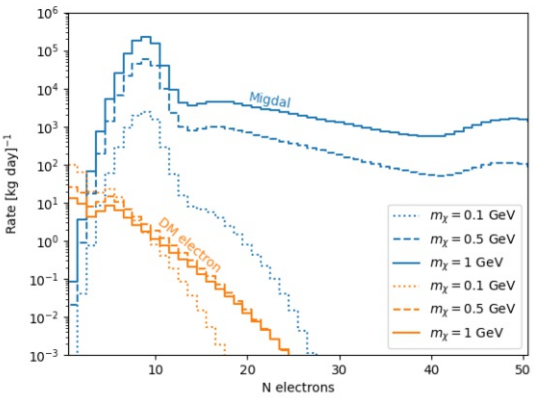

(b) DM-electron scattering (orange) and Migdal effect (blue) as a function of ionization electrons.

Figure 4.4: The overlap of dark matter electron scattering rate and the ionization rate due to the Migdal effect as a function of energy (a) and a function of ionization electrons (b). The cross section is fixed to $\sigma = 10^{-36}$ cm^2, while the dark matter mass varies from $m_\chi = 0.1$ GeV/c^2 to $m_\chi = 1$ GeV/c^2. The overlap extends across almost the entire DM-electron scattering spectrum. Note, that the energy axis on the left side is logarithmic, while the distinct threshold in Migdal rate is dependent of the considered orbitals, which can be seen in figure 2.6.

lation responses – namely their S1 and S2 signal – are shown in in figure 4.2. Using current astrophysical constraints and the secondary ionization model described in 3.1 brought forward by the NEST collaboration (see [122]) nucleus scattering as in the WIMP-paradigm dominates the intrinsic detector response from masses ~ 2 GeV/c^2, however following figure 4.5, neither DM-electron scattering nor the Migdal effect are negligible. The argument that was made for DM-electron scattering and the Migdal effect leaving an overlap in their detector response for low masses is sharpened for masses above ~ 2 GeV/c^2, since there is a rather extensive energy-region, where all the discussed effects cause notable detector responses for all kind of dark matter masses m_χ and interaction cross sections σ. This tendency is already visible in the energy trend of the rates shown in figure 4.5 (upper panel) and very distinct for the initial detector response shown in the lower panel.

Given that we expect a large hierarchy between cross sections to obtain comparable rates, figure 4.5 could also be interpreted as an analysis of the hierarchy between DM-nucleus scattering, the Migdal effect and DM-electron scattering. Also the corresponding ionization rates are shown. In principle these figures prove that one could obtain simultaneously comparable rates if underlying dark matter models have sufficiently different cross sections for each process.

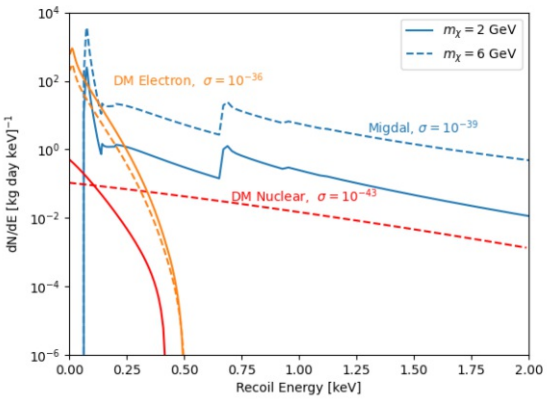

(a) Rates as a function of recoil energy for $m\chi = 2$ GeV/c^2 (solid) and $m\chi = 6$ GeV/c^2 (dashed).

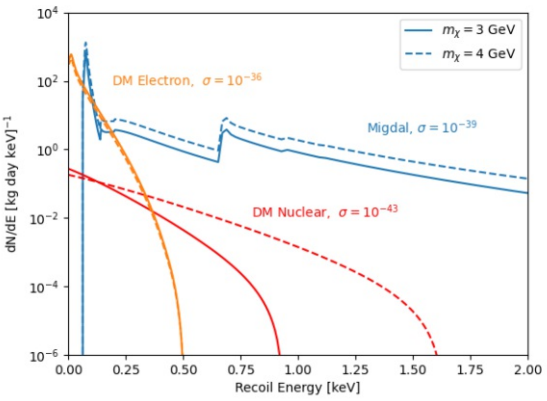

(b) Rates as a function of recoil energy for $m\chi = 3$ (solid) GeV/c^2 and $m\chi = 4$ GeV/c^2 (dashed).

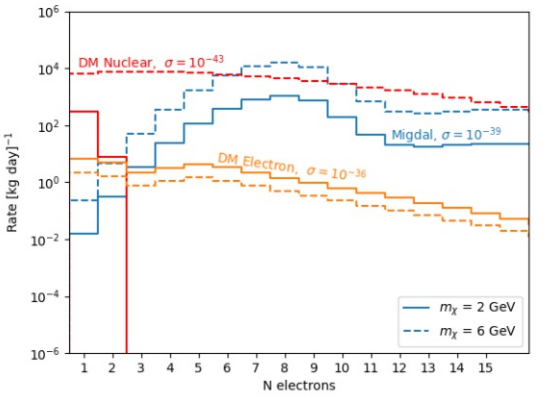

(c) Rates as a function of ionization electrons for $m\chi = 2$ GeV/c^2 (solid) and $m\chi = 6$ GeV/c^2 (dashed).

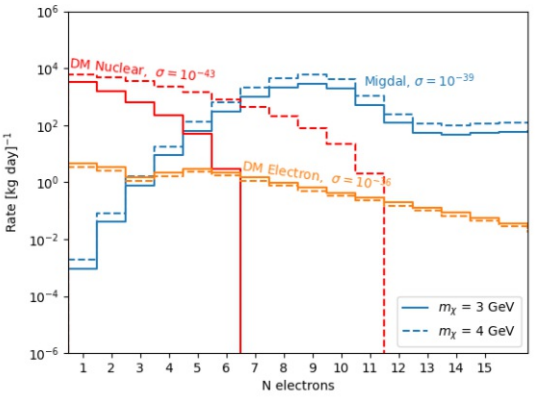

(d) Rates as a function of ionization electrons for $m\chi = 2$ GeV/c^2 (solid) and $m\chi = 6$ GeV/c^2 (dashed).

Figure 4.5: The overlap of all the discussed interactions – dark matter electron scattering rate (orange), ionization rate caused by the Migdal effect (blue) and dark matter nucleus scattering (red) – for different dark matter particle masses and interaction cross sections. The upper panel shows the corresponding rates as a function energy, the lower panel as a function of electrons. The graphs serve two different illustrative purposes, the masses $m\chi = 2$ GeV/c^2 and $m\chi = 6$ GeV/c^2 (a) and (c) show a superposition, even if there are large discrepancies in mass, with the corresponding cross sections ($\sigma = 10^{-36}$ for DM-electron scattering, $\sigma = 10^{-39}$ for the Migdal effect and $\sigma = 10^{-43}$ for DM-nucleus scattering), while the masses $m\chi = 3$ GeV/c^2 and $m\chi = 4$ GeV/c^2 (b) and (d) show the maximal overlap for the same values of σ.

4.3 Energy Overlaps in Semi-Conductors

Similar overlaps are confirmed for semi-conductors, as presented in figure 4.6. It can be seen that the rates for electron scattering in semi-conductors are higher by a factor of about ~ 100 and that the whole electron spectrum is overlaid with nucleus scattering. It must be admitted, however, that this comparison is rather crude compared to the spectra presented for xenon because no initial detector response but only energy spectra are compared. Future work should implement a model for secondary ionization within semi-conductors after some dark matter nuclear recoil. This could then be compared to the already established ionization spectra for electron recoils presented in figure 3.5. It would be even more interesting to investigate the Migdal effect within semiconductors as suggested by [63]. This is discussed in section 5.1.

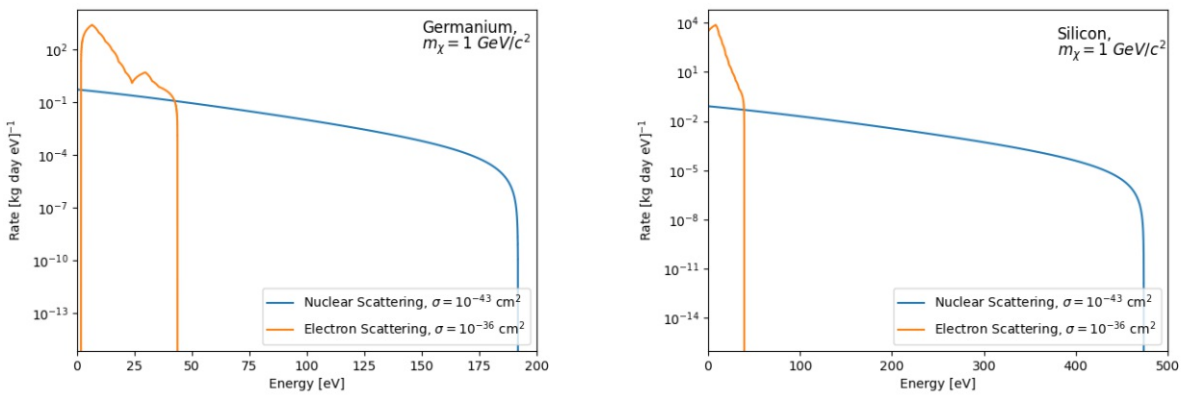

(a) Germanium (b) Silicon

Figure 4.6: The overlap of rates due to dark matter nuclear and dark matter electron scattering for germanium (a) and silicon (b). The mass is fixed to $m\chi = 1$ GeV/c^2, the interaction cross section for nucleus scattering is fixed to $\sigma_n = 10^{-43}$ cm^2, the one for electron scattering to $\sigma_e = 10^{-36}$ cm^2.

Chapter 5

Discussion and Outlook

The aim of this thesis is to raise attention for a problem of current discourse on dark matter direct detection experiments by on the one hand giving weakly interacting massive particles (WIMPs) as Elizabeth Gibney puts it "a final chance to reveal itself" [71], while, on the other hand, reaching out for candidates beyond the WIMP-paradigm. This problem, which might seem trivial at first glance, is substantial for future direct detection experiments, pointing to nothing less but the fact that the cross section limits which are set on the basis of current direct detection experiments are only as reliable as the underlying theory of dark matter and its interaction with target materials. Competing and contradictory interaction theories and new degrees of freedom due to the possibility of there being multiple dark matter components suggest new strategies for the interpretation of experimental data.
This thesis shows distinctive overlaps of different interactions between dark matter and Standard Model particles in mass and energy regime for the concrete example of liquid xenon (chapter 4). Considering a dark matter halo consisting of particles for which none of these interactions are ruled out, this leads to signals within the detector where the underlying interaction remains unknow. Yet, while it would not affect current exclusion limits, it could be a limitation to determine supposed properties of possibly detected dark matter for certain scenarios. The effects discussed in this work are dark matter nucleus scattering, dark matter electron scattering and the Migdal effect, the discussed target being primarily xenon. The overlaps computed for these effects within Xenon suggest similar results for other materials.

5.1 Considering further Effects and Materials

To the extent possible in this work, a variety of current detection experiments and their anticipated signals due to three different interactions were discussed. For a comprehensive

analysis, further target materials and physical interactions should be considered. First of all, this work did not consider the inelastic photon emission from the nucleus in form of *Bremsstrahlung* which is however promising for detecting low-mass dark matter through nuclear recoils, as shown by [87].
In [63] it is pointed out that the theoretical description of the Migdal effect is tied to a scenario of dark matter scattering on single, isolated atoms. It is assumed that this gives correct results for inner-shell electrons within liquid noble gases. Yet, for outer shells it is more subtle: as discussed above, it is assumed that the calculations are valid approximations for outer-shell electrons for liquid noble gases (this is the reason why the $n = 5$ shell was not added to the final signal), but the electronic band structure for semiconductor targets and the complex chemical binding for scintillating crystals definitely requires a different approach. One suggestion is made in [63], another in [92]. This would allow to calculate ionization probabilities as shown in figure 2.6. Taking into account these approaches for solid state targets could crucially extend their sensibility. Ionization form factors for solid state targets could be calculated via QUANTUM ESPRESSO [69] [70], form factors of atoms as in liquid noble gases could be calculated as described in equation 2.18 [60]. Calculating these quantities for other target materials would allow the creation of a detailed map of the detector rates for the leading direct detection experiments and the effects discussed.

5.1.1 Probing concrete multiple component Models

From a theoretical point of view this framework allows to calculate the anticipated detector spectrum of different concrete multiple component dark matter models. If the interaction type and the mass-spectrum as well as the relic density $\Omega_{\chi,i}$ are given, this framework allows to calculate the ionization and scintillation spectrum within a xenon detector (other target materials could easily be implemented). By systematically comparing these spectra with "classical" WIMP spectra, a sensitivity for multiple components of one or more experiments could be determined. This could give further arguments for the combination of different target materials and direct detection experiments. Since each experiment has a different sensitivity for different dark matter masses and interactions, two experiments are possibly able to distinguish what one experiment can not.

Bibliography

[1] G. Aad and et al. Search for new Phenomena in Events with a Photon and Missing Transverse Momentum in pp Collisions at $\sqrt{(s)} = 8$ TeV with the ATLAS detector. *Physical review. D, Particles, fields, gravitation, and cosmology*, 91, 2015.

[2] J. Aalbers, B. Pelssers, and K. D. Morå. *wimprates: v0.3.0*, Jul 2019.

[3] C. E. Aalseth and et al. DarkSide-20k: A 20 Tonne two-phase LAr TPC for Direct Dark Matter Detection at LNGS. *The European Physical Journal Plus*, 133(3), Mar 2018.

[4] M. G. Aartsen and et al. Search for Dark Matter Annihilations in the Sun with the 79-String IceCube Detector. *Physical Review Letters*, 110:131302, Mar 2013.

[5] A. H. Abdelhameed and et al. Description of CRESST-III Data. arXiv 1905.07335.

[6] A. H. Abdelhameed and et al. First Results from the CRESST-III low-mass Dark Matter Program. *Phys. Rev. D*, 100:102002, Nov 2019.

[7] K. Abe, K. Hiraide, K. Ichimura, Y. Kishimoto, K. Kobayashi, M. Kobayashi, S. Moriyama, M. Nakahata, T. Norita, H. Ogawa, and et al. A direct dark matter search in xmass-i. *Physics Letters B*, 789:45–53, Feb 2019.

[8] C. Abel and et al. Measurement of the Permanent Electric Dipole Moment of the Neutron. *Physical Review Letters*, 124:081803, Feb 2020.

[9] O. Abramoff, L. Barak, I. M. Bloch, L. Chaplinsky, M. Crisler, Dawa, A. Drlica-Wagner, R. Essig, J. Estrada, E. Etzion, and et al. "sensei: Direct-detection constraints on sub-gev dark matter from a shallow underground run using a prototype skipper ccd". *Physical Review Letters*, 122(16), Apr 2019.

[10] I. Adachi and et al. Search for an Invisibly Decaying $Z^{'}$ Boson at Belle II in $e^+e^- \to \mu^+\mu^-(e^\pm\mu^\mp)$ Plus Missing Energy Final States. *Physical Review Letters*, 124:141801, Apr 2020.

[11] P. A. R. Ade and et al. Planck 2013 Results. XVI. Cosmological Parameters. *A&A*, 571:A16, 2014.

[12] G. Adhikari and et al. Search for a dark matter-induced annual modulation signal in nai(tl) with the COSINE-100 experiment. *Physical Review Letters*, 123:031302, Jul 2019.

[13] P. Adhikari, R. Ajaj, D. Auty, C. Bina, W. Bonivento, M. Boulay, M. Cadeddu, B. Cai, M. Cárdenas-Montes, S. Cavuoti, and et al. Constraints on dark matter-nucleon effective couplings in the presence of kinematically distinct halo substructures using the deap-3600 detector. *Physical Review D*, 102(8), Oct 2020.

[14] R. Agnese and et al. Search for low-mass weakly interacting massive particles using voltage-assisted calorimetric ionization detection in the supercdms experiment. *Physical Review Letters*, 112:041302, Jan 2014.

[15] R. Agnese and et al. Search for low-mass weakly interacting massive particles with supercdms. *Physical Review Letters*, 112(24), Jun 2014.

[16] R. Agnese and et al. Projected sensitivity of the supercdms snolab experiment. *Phys. Rev. D*, 95:082002, Apr 2017.

[17] D. Akerib, S. Alsum, H. Araújo, X. Bai, A. Bailey, J. Balajthy, P. Beltrame, E. Bernard, A. Bernstein, T. Biesiadzinski, and et al. Results from a search for dark matter in the complete lux exposure. *Physical Review Letters*, 118(2), Jan 2017.

[18] C. Amole and et al. Dark matter search results from the PICO-2L c_3f_8 bubble chamber. *Physical Review Letters*, 114:231302, Jun 2015.

[19] C. Amole and et al. Dark matter search results from the complete exposure of the pico-60 c_3f_8 bubble chamber. *Phys. Rev. D*, 100:022001, Jul 2019.

[20] G. Angloher and et al. Results from 730 kg days of the CRESST-II dark matter search. *The European physical journal. C, Particles and fields*, 72(4):1–22, 2012.

[21] E. Aprile, J. Aalbers, F. Agostini, M. Alfonsi, L. Althueser, F. Amaro, V. Antochi, E. Angelino, F. Arneodo, D. Barge, and et al. A search for light dark matter interactions enhanced by the migdal effect or bremsstrahlung in xenon1t. *Physical Review Letters*, 123(24), Dec 2019.

[22] E. Aprile, J. Aalbers, F. Agostini, M. Alfonsi, F. D. Amaro, M. Anthony, L. Arazi, F. Arneodo, C. Balan, P. Barrow, and et al. Physics reach of the xenon1t dark matter experiment. *Journal of Cosmology and Astroparticle Physics*, 2016(04):027–027, Apr 2016.

[23] E. Aprile, A. E. Bolotnikov, A. I. Bolozdynya, and T. Doke. *Noble Gas Detectors*. Wiley-VCH, Hoboken, 1. aufl. edition, 2007.

[24] E. Aprile and T. Doke. Liquid xenon detectors for particle physics and astrophysics. *Reviews of Modern Physics*, 82(3):2053–2097, Jul 2010.

[25] E. Aprile and et al. XENON1T dark matter data analysis: Signal and background models and statistical inference. *Physical Review D*, 99(11).

[26] E. Aprile and et al. The XENON100 Dark Matter experiment. *Astroparticle physics*, 35(9):573–590, 2012.

[27] E. Aprile et al. Search for Light Dark Matter Interactions Enhanced by the Migdal Effect or Bremsstrahlung in XENON1T. *Physical Review Letters*, 123(24):241803, 2019.

[28] E. Aprile et al. XENON1T Dark Matter data analysis: Signal and background models and statistical inference. *Phys. Rev. D*, 99(11):112009, 2019.

[29] E. Aprile and et al. Search for inelastic scattering of WIMP Dark Matter in XENON1T, 2020.

[30] E. Aprile, K. L. Giboni, P. Majewski, K. Ni, and M. Yamashita. Observation of Anticorrelation between Scintillation and Ionization for MeV Gamma Rays in Liquid Xenon. *Physical Review B*, 76(1), Jul 2007.

[31] E. Armengaud and et al. Performance of the EDELWEISS-III Experiment for Direct Dark Matter Searches. *Journal of Instrumentation*, 12(08):P08010–P08010, Aug 2017.

[32] Y. Ascasibar, P. Jean, C. Bœhm, and J. Knödlseder. Constraints on Dark Matter and the shape of the Milky Way dark halo from the 511-keV line. *Monthly Notices of the Royal Astronomical Society*, 368(4):1695–1705, Apr 2006.

[33] E. Barbosa de Souza and et al. First Search for a Dark Matter Annual Modulation Signal with NaI(Tl) in the Southern Hemisphere by DM-Ice17. *Phys. Rev. D*, 95:032006, Feb 2017.

[34] J. Barreto and et al. Direct Search for Low mass Dark Matter Particles with CCDs. *Physics Letters B*, 711(3):264 – 269, 2012.

[35] D. Baxter, Y. Kahn, and G. Krnjaic. Electron Ionization via Dark Matter-Electron Scattering and the Migdal Effect. *Physical Review D*, 101(7), Apr 2020.

[36] J. Bekenstein and M. Milgrom. Does the missing mass problem signal the breakdown of Newtonian gravity? *The Astrophysical Journal*, 286:7–14, Nov 1984.

[37] R. Bernabei and et al. Investigating Electron Interacting Dark Matter. *Physical Review D*, 77(2), Jan 2008.

[38] R. Bernabei and et al. Final model independent result of dama/libra-phase1. *The European physical journal. C, Particles and fields*, 73(12), 2013.

[39] G. Bertone. *Particle Dark Matter: Observations, Models and Searches*. Cambridge University Press, Cambridge, 2010.

[40] G. Bertone and D. Hooper. History of Dark Matter. *Reviews of Modern Physics*, 90(4), Oct 2018.

[41] S. Bhattacharya, A. Drozd, B. Grzadkowski, and J. Wudka. Two-component Dark Matter. *Journal of High Energy Physics*, 2013(10), Oct 2013.

[42] T. Bringmann, X. Huang, A. Ibarra, S. Vogl, and C. Weniger. Fermi LAT Search for Internal Bremsstrahlung Signatures from Dark Matter Annihilation. *Journal of Cosmology and Astroparticle Physics*, 2012(07):054–054, Jul 2012.

[43] G. Bélanger, A. Pukhov, C. Yaguna, and O. Zapata. The Z_5 Model of Two-Component Dark Matter. arXiv 2006.14922, 2020.

[44] G. Bélanger, A. Pukhov, C. Yaguna, and O. Zapata. The z_5 model of two-component dark matter, 2020.

[45] Chandra-Satellite. Photo Album – 1E 0657-56 - 21. `https://en.wikipedia.org/w/index.php?title=Galaxy_rotation_curve&oldid=701684941`, Jul 2020. Last retrieved 2020-07-25.

[46] Chandra-Satellite. Rotation curve of the m33 cluster. `https://chandra.harvard.edu/photo/2006/1e0657/index.html`, Jul 2020. Last retrieved 2020-07-27.

[47] S. Chatrchyan et al. The CMS Experiment at the CERN LHC. *JINST*, 3:S08004, 2008.

[48] K. Choi and et al. Search for Neutrinos from Annihilation of Captured Low-Mass Dark Matter Particles in the Sun by Super-Kamiokande. *Physical Review Letters*, 114:141301, Apr 2015.

[49] D. Clowe, M. Bradač, A. H. Gonzalez, M. Markevitch, S. W. Randall, C. Jones, and D. Zaritsky. A Direct Empirical Proof of the Existence of Dark Matter. *The Astrophysical Journal*, 648(2):L109–L113, Aug 2006.

[50] E. Corbelli and P. Salucci. The extended Rotation Curve and the Dark Matter Halo of M33. *Monthly Notices of the Royal Astronomical Society*, 311(2):441–447, Jan 2000.

[51] X. Cui and et al. Dark Matter Results from 54-Ton-Day Exposure of PandaX-II Experiment. *Physical Review Letters*, 119:181302, Oct 2017.

[52] T. Doke, H. J. Crawford, A. Hitachi, J. Kikuchi, P. J. Lindstrom, K. Masuda, E. Shibamura, and T. Takahashi. Let dependence of scintillation yields in liquid argon. *Nuclear Instruments and Methods in Physics Research Section A: Accelerators, Spectrometers, Detectors and Associated Equipment*, 269(1):291 – 296, 1988.

[53] T. Doke and et al. Absolute Scintillation Yields in Liquid Argon and Xenon for Various Particles. *Jap. J. Appl. Phys.*, 41:1538–1545, 2002.

[54] F. Donato, N. Fornengo, and S. Scopel. Effects of Galactic Dark Halo Rotation on WIMP Direct Detection. *Astroparticle Physics*, 9(3):247 – 260, 1998.

[55] G. Dūda, A. Kemper, and P. Gondolo. Model-independent Form Factors for spin-independent Neutralino–Nucleon Scattering from elastic Electron Scattering Data. *Journal of Cosmology and Astroparticle Physics*, 2007(04):012–012, Apr 2007.

[56] F. W. Dyson, A. S. Eddington, and C. Davidson. A Determination of the Deflection of Light by the Sun's Gravitational Field, from Observations Made at the Total Eclipse of May 29, 1919. *Philosophical Transactions of the Royal Society of London. Series A, Containing Papers of a Mathematical or Physical Character*, (220291–333), Jan 1920.

[57] J. Einasto. Dark Matter. *Brazilian Journal of Physics*, 43(5-6):369–374, 2013.

[58] A. Einstein. *Kosmologische Betrachtungen zur allgemeinen Relativitätstheorie*, pages 119–130. John Wiley & Sons, Ltd, 2006.

[59] R. Essig, M. Fernandez-Serra, J. Mardon, A. Soto, T. Volansky, and T.-T. Yu. Direct Detection of sub-GeV Dark Matter with Semiconductor Targets. arXiv 1509.01598, 2016.

[60] R. Essig, A. Manalaysay, J. Mardon, P. Sorensen, and T. Volansky. First Direct Detection Limits on Sub-GeV Dark Matter from XENON10. *Physical Review Letters*, 109(2), Jul 2012.

[61] R. Essig, A. Manalaysay, J. Mardon, P. Sorensen, and T. Volansky. First Direct Detection Limits on sub-GeV Dark Matter from XENON10. *Physical Review Letters*, 109:021301, 2012.

[62] R. Essig, J. Mardon, and T. Volansky. Direct Detection of Sub-GeV Dark Matter. *Phys. Rev. D*, 85:076007, 2012.

[63] R. Essig, J. Pradler, M. Sholapurkar, and T.-T. Yu. Relation between the Migdal Effect and Dark Matter-Electron Scattering in Isolated Atoms and Semiconductors. *Physical Review Letters*, 124:021801, Jan 2020.

[64] R. Essig, T. Volansky, and T.-T. Yu. New Constraints and Prospects for sub-GeV Dark Matter Scattering off Electrons in Xenon. *Phys. Rev. D*, 96(4):043017, 2017.

[65] D. P. Finkbeiner and N. Weiner. Exciting Dark Matter and the INTEGRAL/SPI 511 keV signal. *Phys. Rev. D*, 76:083519, Oct 2007.

[66] D. J. Fixsen. The Temperature of the Cosmic Microwave Background. *The Astrophysical Journal*, 707(2):916–920, Nov 2009.

[67] J. M. Gaskins. A Review of Indirect Searches for Particle Dark Matter. *Contemporary physics*, 57(4):496–525, 2016.

[68] G. B. Gelmini, E. Osoba, and S. Palomares-Ruiz. Inert-sterile Neutrino: Cold or warm Dark Matter Candidate. *Physical Review D*, 81(6), Mar 2010.

[69] P. Giannozzi and et al. QUANTUM ESPRESSO: A modular and open-source Software Project for Quantum Simulations of Materials. *Journal of Physics: Condensed Matter*, 21(39):395502 (19pp), 2009.

[70] P. Giannozzi and et al. Advanced Capabilities for Materials modelling with Quantum ESPRESSO. *Journal of Physics: Condensed Matter*, 29(46):465901, Oct 2017.

[71] E. Gibney. Last chance for WIMPs: Physicists launch all-out Hunt for Dark-Matter Candidate. *Nature (London)*, 586(7829):344, 2020.

[72] D. A. Glaser. Some Effects of Ionizing Radiation on the Formation of Bubbles in Liquids. *Phys. Rev.*, 87:665–665, Aug 1952.

[73] M. W. Goodman and E. Witten. Detectability of certain Dark-Matter Candidates. *Phys. Rev. D*, 31:3059–3063, Jun 1985.

[74] O. y. Grø n. *Einstein's General Theory of Relativity: With Modern Applications in Cosmology*. Springer, New York, NY [u.a.], 2007.

[75] F. Hasenbalg, D. Abriola, J. I. Collar, D. E. Di Gregorio, A. O. Gattone, H. Huck, D. Tomasi, and I. Urteaga. Cold dark matter identification: Diurnal modulation re-examined. *Physical Review D*, 55(12):7350–7355, Jun 1997.

[76] R. H. Helm. Inelastic and elastic scattering of 187-mev electrons from selected even-even nuclei. *Phys. Rev.*, 104:1466–1475, Dec 1956.

[77] E. Hubble. A relation between distance and radial velocity among extra-galactic nebulae. *Proceedings of the National Academy of Sciences*, 15(3):168–173, 1929.

[78] M. Ibe, W. Nakano, Y. Shoji, and K. Suzuki. Migdal Effect in Dark Matter Direct Detection Experiments. *Journal of High Energy Physics*, 2018(3), Mar 2018.

[79] M. Ibe, W. Nakano, Y. Shoji, and K. Suzuki. Migdal Effect in Dark Matter Direct Detection Experiments. *JHEP*, 03:194, 2018.

[80] J. H. Jeans. The Motions of Stars in a Kapteyn-Universe. *Monthly Notices of the Royal Astronomical Society*, 82(3):122–132, 1922.

[81] G. Jungman, M. Kamionkowski, and K. Griest. Supersymmetric Dark Matter. *Physics Reports*, 267(5):195 – 373, 1996.

[82] J. C. Kapteyn. First Attempt at a Theory of the Arrangement and Motion of the Sidereal System. *The Astrophysical Journal*, 55:302, 1922.

[83] J. E. Kim and G. Carosi. Axions and the strong *CP* Problem. *Rev. Mod. Phys.*, 82:557–601, Mar 2010.

[84] C. A. Klein. Bandgap Dependence and Related Features of Radiation Ionization Energies in Semiconductors. *Journal of applied physics*, 39(4):2029–2038, 1968.

[85] H. Kluck, A. Bähr, J. Ninkovic, J. Schieck, H. Shi, and J. Treis. "danae: A new effort to directly search for dark matter with depfet-rndr detectors". *Nuclear Instruments and Methods in Physics Research Section A: Accelerators, Spectrometers, Detectors and Associated Equipment*, 958:162155, 2020. Proceedings of the Vienna Conference on Instrumentation 2019.

[86] J. Kopp, V. Niro, T. Schwetz, and J. Zupan. DAMA/LIBRA data and leptonically interacting Dark Matter. *Physical Review D*, 80(8), Oct 2009.

[87] C. Kouvaris and J. Pradler. Probing Sub-GeV Dark Matter with Conventional Detectors. *Physical Review Letters*, 118(3), Jan 2017.

[88] S. Lee, B. Kilminster, and A. Macchiolo. Dark matter in ccds at modane (damic-m): a silicon detector apparatus searching for low-energy physics processes. *Journal of instrumentation*, 15(2):C02050–C02050, 2020.

[89] G. Lemaître. Un Univers homogène de Masse constante et de Rayon croissant rendant compte de la Vitesse radiale des Nébuleuses extra-galactiques. *Annales de la Société Scientifique de Bruxelles*, 47:49–59, Jan 1927.

[90] J. Lewin and P. Smith. Review of Mathematics, numerical Factors, and Corrections for Dark Matter Experiments based on Elastic Nuclear Recoil. *Astroparticle Physics*, 6(1):87 – 112, 1996.

[91] P. Li, F. Lelli, S. McGaugh, and J. Schombert. A comprehensive catalog of dark matter halo models for sparc galaxies. *The Astrophysical Journal Supplement Series*, 247(1):31, Mar 2020.

[92] Z.-L. Liang, L. Zhang, P. Zhang, and F. Zheng. Describing Migdal Effects in Diamond Crystal with atom-centered localized Wannier Functions. Dec 2019.

[93] B. Lindblad. *Uppsala Meddelanden 11*, page 30f. University of Uppsala, 1926.

[94] J. Lindhard, V. Nielsen, M. Scharff, and P. V. Thomsen. Integral Equations governing Radiation Effects. (Notes on atomic Collisions III). *Kgl. Danske Videnskab., Selskab. Mat. Fys. Medd.*, Vol: 33: No. 10(10), Jan 1963.

[95] H. Ma, Y. Chen, Q. Yue, L. Wang, T. Xue, Z. Zeng, K. Kang, J. Cheng, Y. Li, J. Li, and et al. Cdex dark matter experiment: Status and prospects. *Journal of Physics: Conference Series*, 1342:012067, Jan 2020.

[96] D. Malling and C. Faham. Large underground xenon experiment. `https://en.wikipedia.org/wiki/File:LUXEvent.pdf`, Sep 2020. Last retrieved 2020-09-12.

[97] A. B. Migdal. Bremsstrahlung and Pair Production in Condensed Media at High Energies. *Phys. Rev.*, 103:1811–1820, Sep 1956.

[98] V. B. Mikhailik and H. Kraus. Cryogenic scintillators in searches for extremely rare events. *Journal of Physics D: Applied Physics*, 39(6):1181–1191, Mar 2006.

[99] S. Mitra. Has dama detected self-interacting dark matter? *Physical Review D*, 71(12), Jun 2005.

[100] NEST-Collaboration. Benchmark plots. `http://nest.physics.ucdavis.edu/benchmark-plots`, Oct 2020. Last retrieved 2020-10-28.

[101] K. Ni, E. Aprile, K. L. Giboni, P. Majewski, and M. Yamashita. Gamma ray spectroscopy with scintillation light in liquid xenon. *Journal of Instrumentation*, 1(09):P09004–P09004, Sep 2006.

[102] J. Oort. The Force exerted by the Stellar System in the Direction Perpendicular to the galactic Plane and some related Problems. *Bulletin of the Astronomical Institutes of the Netherlands*, 1932.

[103] A. A. Penzias. Free Hydrogen in the Pegasus I Cluster of Galaxies. *The Astronomical Journal*, 66:293, 1961.

[104] A. A. Penzias and R. W. Wilson. A measurement of excess antenna temperature at 4080 mc/s. *The Astrophysical Journal*, 142:419–421, Jul 1965.

[105] S. Perlmutter and et al. Discovery of a supernova explosion at half the age of the universe. *Nature (London)*, 391(6662):51–54, 1998.

[106] H. Poincaré. The Milky Way and the Theory of Gases. In *The Foundations of Science: Science and Hypothesis, The Value of Science, Science and Method*, pages 523–534. Cambridge University Press, 2014.

[107] M. Pospelov and A. Ritz. The Galactic 511 keV Line from Electroweak Scale WIMPs. *Physics Letters B*, 651(2-3):208–215, Jul 2007.

[108] S. Profumo, K. Sigurdson, and L. Ubaldi. Can we discover dual-component thermal wimp dark matter? *Journal of Cosmology and Astroparticle Physics*, 2009(12):016–016, Dec 2009.

[109] F. Reindl. *Exploring Light Dark Matter With CRESST-II Low-Threshold Detectors*. PhD thesis, Munich, Tech. U., 2016.

[110] A. G. Riess and et al. Observational Evidence from Supernovae for an Accelerating Universe and a Cosmological Constant. *The Astronomical Journal*, 116(3):1009–1038, Sep 1998.

[111] V. C. Rubin and J. Ford, W. Kent. Rotation of the Andromeda Nebula from a Spectroscopic Survey of Emission Regions. *The Astrophysical Journal*, 159:379, Feb 1970.

[112] S. E. Rugh and H. Zinkernagel. The Quantum Vacuum and the Cosmological Constant Problem, 2001.

[113] R. K. Sachs and A. M. Wolfe. Perturbations of a Cosmological Model and Angular Variations of the Microwave Background. *Astro*, 147:73, Jan 1967.

[114] C. Savage, G. Gelmini, P. Gondolo, and K. Freese. Compatibility of dama/libra dark matter detection with other searches. *Journal of Cosmology and Astroparticle Physics*, 2009(04):010–010, Apr 2009.

[115] H. Shi, A. Bähr, H. Kluck, J. Ninkovic, J. Schieck, and J. Treis. DANAE - a new experiment for direct dark matter detection with DEPFET silicon detectors. *PoS*, ICHEP2018:589, 2019.

[116] T. Shutt, C. Dahl, J. Kwong, A. Bolozdynya, and P. Brusov. Performance and fundamental Processes at low Energy in a two-phase liquid Xenon Dark Matter Detector. *Nuclear Instruments and Methods in Physics Research Section A: Accelerators, Spectrometers, Detectors and Associated Equipment*, 579(1):451–453, Aug 2007.

[117] M. C. Smith and et al. The RAVE survey: Constraining the local galactic escape Speed. *Monthly Notices of the Royal Astronomical Society*, 379(2):755–772, Jul 2007.

[118] S. Smith. The Mass of the Virgo Cluster. *The Astrophysical Journal*, 83:23, Jan 1936.

[119] P. Sorensen and C. E. Dahl. Nuclear recoil energy scale in liquid xenon with application to the direct detection of dark matter. *Physical Review D*, 83(6), Mar 2011.

[120] B. G. Streetman. *Solid State electronic Devices*. Prentice-Hall Series in Solid State physical Electronics. Prentice-Hall, Englewood Cliffs, NJ, 2. ed., 2. [print.]. edition, 1980.

[121] M. Szydagis and et al. NEST: A Comprehensive Model for Scintillation Yield in Liquid Xenon. *Journal of Instrumentation*, 6(10).

[122] M. Szydagis and et al. NEST collaboration. `http://nest.physics.ucdavis.edu/`, Oct 2020. Last retrieved 2020-10-28.

[123] M. Szydagis, A. Fyhrie, D. Thorngren, and M. Tripathi. Enhancement of NEST Capabilities for Simulating low-energy Recoils in liquid Xenon. *Journal of Instrumentation*, 8(10):C10003–C10003, Oct 2013.

[124] M. Tanabashi. and et al. Review of Particle Physics. *Phys. Rev.*, 98:Chapter 26, Dec 2018 and 2019 update.

[125] J. Thomas and D. A. Imel. Recombination of Electron-Ion Pairs in liquid Argon and liquid Xenon. *Phys. Rev. A*, 36:614–616, Jul 1987.

[126] W. Thomson, Baron Kelvin. *Baltimore Lectures on Molecular Dynamics and the Wave Theory of Light*. Cambridge library collection. Physical Sciences. Baltimore, 1904.

[127] J. Tiffenberg, M. Sofo-Haro, A. Drlica-Wagner, R. Essig, Y. Guardincerri, S. Holland, T. Volansky, and T.-T. Yu. "single-electron and single-photon sensitivity with a silicon skipper ccd". *Physical Review Letters*, 119(13), Sep 2017.

[128] P. Tisserand, L. Le Guillou, C. Afonso, J. N. Albert, J. Andersen, R. Ansari, Aubourg, P. Bareyre, J. P. Beaulieu, X. Charlot, and et al. Limits on the macho content of the galactic halo from the eros-2 survey of the magellanic clouds. *Astronomy Astrophysics*, 469(2):387–404, Apr 2007.

[129] Q. Wang and et al. Results of Dark Matter Search using the Full PandaX-II Exposure. arXiv 2007.15469, 2020.

[130] G. Weidenspointner and et al. The Sky Distribution of 511 keV Positron Annihilation line Emission as measured with INTEGRAL/SPI. *European Space Agency, (Special Publication) ESA SP*, 2007.

[131] H. T.-K. Wong. Taiwan EXperiment On NeutrinO History and Prospects. *The Universe*, 3(4):22–37, 2015.

[132] N. J. Woolf. On the Stabilization of Clusters of Galaxies by Ionized Gas. *The Astrophysical Journal*, 148:287, Apr 1967.

[133] S. Yellin. Finding an upper Limit in the Presence of an unknown Background. *Physical Review D*, 66(3), Aug 2002.

[134] S. Yellin. Software for computing an upper limit given unknown background. `http://titus.stanford.edu/Upperlimit/`, Feb 2011. Last retrieved 2020-10-03.

[135] T.-T. Yu and et al. Direct Detection of Light Dark Matter. `http://ddldm.physics.sunysb.edu/ddlDM/`, 2011.

[136] H. Yüksel. Positron Annihilations at the Galactic Center: Generating More Questions Than Answers", journal = "Nuclear Physics B - Proceedings Supplements. 173:83 – 86, 2007. Proceedings of the 7th UCLA Symposium on Sources and Detection of Dark Matter and Dark Energy in the Universe.

[137] K. M. Zurek. Multicomponent dark matter. *Physical Review D*, 79(11), Jun 2009.

[138] F. Zwicky. Die Rotverschiebung von extragalaktischen Nebeln. *Helvetica Physica Acta*, 6(II):110, 1933.

[139] F. Zwicky. On the Masses of Nebulae and of Clusters of Nebulae. *The Astrophysical Journal*, 86:217, Oct 1937.

[140] E. Öpik. Selective Absorption of Light in Space, and the Dynamics of the Universe. In *Bull. de la Soc. Astr. de Russie*, pages 150–158. Soc. Astr. de Russie, 1915.

List of Figures